Applied Catalysis B: Environmental 296 (2021) 120371

Contents lists available at ScienceDirect

Applied Catalysis B: Environmental

journal homepage: www.elsevier.com/locate/apcatb

Improved interface compatibility of hollow H-$Zr_{0.1}Ti_{0.9}O_2$ with UiO-66-NH_2 *via* Zr-Ti bidirectional penetration to boost visible photocatalytic activity for acetaldehyde degradation under high humidity

Peng Hu [a,b], Ruimeng Wang [a], Zhu Gao [a,c], Shanliang Jiang [a], Zhongxing Zhao [a], Hongbing Ji [a,b,d,**], Zhenxia Zhao [a,*]

[a] School of Chemistry and Chemical Engineering, MOE Key Laboratory of New Processing Technology for Nonferrous Metals and Materials, Guangxi Key Laboratory of Processing for Nonferrous Metals and Featured Materials, Guangxi University, Nanning, 530004, China
[b] Fine Chemical Industry Research Institute, School of Chemistry, Sun Yat-Sen University, Guangzhou, 510275, China
[c] School of Chemistry and Chemical Engineering, Central South University, Changsha, 410083, China
[d] School of Chemical Engineering, Guangdong University of Petrochemical Technology, Maoming, 525000, China

ARTICLE INFO

Keywords:
Interface compatibility
Hollow H-$Zr_{0.1}Ti_{0.9}O_2$@U6N
Zr-Ti bidirectional penetration
CH_3CHO photodegradation
High humidity

ABSTRACT

Well-defined construction of interface compatibility is greatly helpful to overcome interface attenuation, featuring the combined advantages from different photo-catalysts. Herein, we proposed "Interfacial metal interpenetration" strategy to engineer a novel hetero-structural TiO_x@UiO-66-NH_2 photocatalyst (H-$Zr_{0.1}Ti_{0.9}O_2$@U6N) having core-shell characters and well-organized interface compatibility for acetaldehyde (ALD) degradation. XRD refinement and XPS showed that Zr and Ti clusters were proved to induce the lattice expansion of H-$Zr_{0.1}Ti_{0.9}O_2$ and lattice shrink of UiO-66-NH_2, respectively. This strategy efficiently overcame transmission jam of photo-induced electrons, facilitating the separation efficiency of electron-holes. Furthermore, improved interface compatibility and hollow merits of H-$Zr_{0.1}Ti_{0.9}$@U6N jointly expedited the mass transfer of reactants, shortening the "adsorption-catalysis" pathway. Therefore, H-$Zr_{0.1}Ti_{0.9}O_2$@U6N showed about two orders of magnitude increase of catalytic kinetics (195×10^{-3} min^{-1}) compared to H-TiO_2 (0.002 min^{-1}) at 75 % relative humidity (RH), far beyond noble metal modified photo-catalyst Ag@TiO_2 (11.9×10^{-3} min^{-1}). The "Interfacial metal interpenetration" strategy can effectively improve material compatibility and award multiplying effects for different photo-catalysts.

1. Introduction

Aldehydes volatile organic compounds (VOCs) are regarded as a group of crucial outdoor/indoor atmospheric contaminants produced by toxic solvents and stored fuels as well as the emission of environmental tobacco smoke [1], being potential threats to environment and human health even under very low concentrations [2]. Aldehydes, a representative poisonous indoor contaminant, will seriously result in healthy illness *i.e.* nasal tumors, skin irritation and nasopharyngeal cancer if staying inside for long time (more than 80 % of daily time indoors) [3]. Hence, the efficient elimination of ALD from microenvironment under low concentrations is of significance and has attracted much concern [4]. Among covered methods, the removal of ALD based on photocatalysis process were known to be a practical and facile strategy due to its clean, cost effectiveness and environmentally friendly strengths [5,6]. For an ideal photocatalysts, it should meet the demands including high visible light efficiency, high charge-separation and long-term reaction stability *etc.* [7,8].

Metal-organic frameworks (MOFs), a well-known class of porous crystalline materials, have been vigorously investigated in the field of gas storage, separation, and photocatalytic reactions [9,10] due to the laudable porous texture, and ultra-high surface area *etc.* [11]. Whereas, the properties of pure MOFs in photocatalysis were usually suppressed by low efficiency in the generation of electrons, low photosensitivity and

* Corresponding author.
** Corresponding author at: School of Chemistry and Chemical Engineering, MOE Key Laboratory of New Processing Technology for Nonferrous Metals and Materials, Guangxi Key Laboratory of Processing for Nonferrous Metals and Featured Materials, Guangxi University, Nanning, 530004, China.
E-mail addresses: jihb@mail.sysu.edu.cn (H. Ji), zhaozhenxia@gxu.edu.cn (Z. Zhao).

https://doi.org/10.1016/j.apcatb.2021.120371
Received 1 February 2021; Received in revised form 3 April 2021; Accepted 13 May 2021
Available online 15 May 2021

deficient electron-holes separation in MOFs [11]. In this regard, numerous MOF-based composite photocatalyst were proved to advance photosensitivity and separation efficiency of carriers through the reasonable construction of interface heterojunction with some semiconductors. For example, Crake et al. synthesized a composited TiO_2/NH_2-UiO-66 through solvothermal method for CO_2 photoreduction [12]. The composites expressed an advanced photocatalytic activity *via* the efficient construction of heterojunction. Ye and co-workers also covered the TiO_2/HKUST-1 materials with the merits of excellent VOCs adsorption and enhanced transmission efficiency of photogenerated carriers [13]. Degradation results showed that TiO_2/HKUST-1 possessed improved photocatalytic degradation efficiency and favorable interface contact. Yet, it should be stressed that the composited photocatalysts usually suffer the following barriers *i.e.* (1) how to optimize the interface compatibility and structure an well-defined interface heterojunction to advance the separation efficiency of carriers and reaction kinetics have always been a research challenge [14]; (2) the morphologies of integrated semiconductors photocatalysts *i.e.* GO and TiO_2 *etc.* usually appeared in the form of aggregated powder or irregular shapes, which limited the light utilization and reduced the mass transfer of reactants and products during catalytic reactions [15]; (3) Their catalytic activity and stability have been suffering negative interference from humid air. Strongly competitive adsorption of water on unsaturated metal sites of MOFs would damage their catalytic activity and stability, which has seriously hindered their practical application.

Given the above-mentioned issues, "hard template" and "Interfacial metal interpenetration" strategies were proposed to engineer a novel hetero-structural TiO_x@UiO-66-NH_2 photocatalyst (termed as H-$Zr_{0.1}Ti_{0.9}O_2$@U6N) having core-shell hollow nanoparticle for LAD degradation. In this work, "Interfacial metal interpenetration" mainly referred to the interpenetrative of Ti and Zr in crystal structure of H-TiO_2 and U6N. That means portion of Zr infiltrated into H-TiO_2, and portion of Ti infiltrated into U6N on the interface of H-$Zr_{0.1}Ti_{0.9}O_2$@U6N. The structured bidirectional penetrated interface of Zr/Ti as metal clusters was proved to appear in both structures of TiO_x and UiO-66-NH_2, which resulted in changes in their crystal lattices and Zr/Ti coordination as verified by XRD refinement and XPS spectra. This unique bidirectional penetrated interface upon Zr/Ti bridging would efficiently overcome the transmission barriers of photo-induced electron and positively boost the separation efficiency of photo-induced carriers. Photocatalytic tests showed that the specific tight-bonding interface and hollow structure not only enabled a faster mass transfer process *via* shortening the reaction pathway, but also contributed ~ 100 times increase of reaction rate for aldehyde degradation with a RH of 75 %. Besides, well-defined hollow structure could impart the hybrids with preferable and advanced utilization of visible light. Thorough analysis of structural characterizations including field emission scanning electron microscope (FE-SEM), X-ray diffraction (XRD) and N_2 adsorption *etc.* as well as the optical tests *i.e.* UV–vis diffuse reflectance spectroscopy (UV-DRS), electrochemical impedance spectroscopy (EIS), surface photovoltage spectroscope (SPS), CO-DRIFS spectra and in-situ KPFM study *etc*. had comprehensively investigated on their corresponding photo-catalysis properties.

2. Experimental section

2.1. Materials and methods

Tetrabutyl titanate (TBOT) ($C_{16}H_{36}O_4Ti$, > 99 %) and 2-aminoterephthalic acid ($C_8H_7NO_4$, > 98 %) were purchased from Sigma, USA. Methyl acrylate ($C_4H_6O_2$, > 99 %), styrene (C_8H_8, > 98 %) and absolute ethanol (C_2H_5OH, 99.7 %) were purchased from Kelong Chemical Reagent Co., Ltd. Chengdu, China. Potassium persulfate ($K_2S_2O_8$, > 99 %), ammonium hydroxide ($NH_3{\cdot}H_2O$, 28 %) and N, N-dimethylformamide (C_3H_7NO, 99.7 %) were purchased from Nanning LanTian Chemical reagent Co. Ltd. Nanning, China. All the chemicals adopted in this work were of commercially available analytical grade and used without purification.

2.2. Synthesis procedure

2.2.1. Synthesis of ultra-small UiO-66-NH_2 nanocrystals under facile conditions

The facile strategy to synthesis UiO-66-NH_2 nanocrystals with subsize was mainly based on two-step procedure according to the covered approach [16]. Originally, 47.3 μL of zirconium propoxide solution and 7 mL of DMF were mixed for 30 min at 298 K, then 1 mL of acetic acid was subsequently added into the 25 mL scintillation vial and then executed the heating procedure at 403 K in the oven to form the Zr clusters, followed by cooling them to room temperature. Next, 0.051 g of 2-aminoterephthalic acid (NH_2-BDC) was added and further stirred at 250 rpm for 18 h at 298 K. Afterwards, the yielding samples were washed and centrifuged with ethanol several times and further were dried at 343 K.

2.2.2. Synthesis of polystyrene microspheres

Polystyrene (PS) microspheres were prepared by a soap-free emulsion polymerization method [17]. Briefly, the polymerization process was carried out in a 250 mL three-necked stirred flask which were equipped with reflux condenser, mechanical stirrer and thermostat water bath device under a N_2 atmosphere. Initially, 100 mL of deionized water was added to the flask and the system were then purification *via* a steam of N_2 to be deoxygenated for 40 min. After that, 10 mL of styrene and 0.52 mL of methyl acrylate were added to the above reactor and kept stirring for 30 min. Soon afterwards, the system temperature was raised to 343 K under a continuous stirring rate of 200 rpm and maintained it for 10 min. Afterwards, the solution of $Na_2S_2O_8$ as an initiator followed by addition dropwise. As the reaction completed, the resulting negative-charged PS microspheres were centrifuged and washed with ethanol several times, respectively. Finally, the resultant powders were dried in conventional oven at the temperature of 333 K.

2.2.3. Synthesis of hollow H-TiO_2 and Zr-engineered H-$Zr_{0.1}Ti_{0.9}O_2$ microspheres

The procedure of hollow H-TiO_2 microspheres was prepared according the modified procedure [17,18]. Typically, the as-prepared PS (~ 0.3 g) were dispersed into the mixed solution including 50 mL of ethanol, followed by adding 1.0 g of cetyltrimethylammonium ammonium bromide (CTAB) and 0.3 mL of ammonium hydroxide. Then the process was stirring for 24 h, 0.25 mL of tetrabutyl titanate (TBOT) was added dropwise to the as-prepared PS suspension solution under vigorous stirring process, and the mixture were continuously agitating for 2 h at 298 K. The products were then washed and centrifuged with EtOH several times to remove residual impurities and then immersed into 40 mL of DMF solvent for 2 h at 298 K. So, the freshly hollow H-TiO_2 microspheres could be facilely synthesized through the solvent etching method to remove the PS [19], followed by the annealing process in N_2 at 573 K for 4 h in the muffle furnace at a heating rate of 280 K/min. The as-prepared samples were collected and denoted as H-TiO_2. For the Zr-engineered H-$Zr_{0.1}Ti_{0.9}O_2$, $ZrCl_4$ was in-situ added with a given molar ratio ($n_{Zr^{4+}}/n_{Ti^{4+}} = 1/10$) in the ethanol solution together with the slowly addition of TBOT (dissolved in 10 mL of ethanol solution), and hereafter maintained the same approach as the prepared course of hollow H-TiO_2.

2.2.4. Synthesis of hollow H-TiO_2@U6N and H-$Zr_{0.1}Ti_{0.9}O_2$@U6N composites

In this procedure, the self-assembly growth technology at room-temperature was proposed for the preparation of H-TiO_2@U6N and H-$Zr_{0.1}Ti_{0.9}O_2$@U6N composites. The linker NH_2-BDC was preferentially added into the suspension of H-TiO_2 and H-$Zr_{0.1}Ti_{0.9}O_2$, respectively, to achieve the superficial carboxylate-terminated H-TiO_2 and H-

$Zr_{0.1}Ti_{0.9}O_2$ particles *via* electrostatic interaction [20]. The prepared H-TiO_2 and H-$Zr_{0.1}Ti_{0.9}O_2$ were further reacted with subsequent adding zirconium clusters to actualize the crystal nucleus growth of ultra-small U6N nanocrystals on the surface of H-TiO_2 and H-$Zr_{0.1}Ti_{0.9}O_2$ microspheres, and the materials were denoted as H-TiO_2@U6N and H-$Zr_{0.1}Ti_{0.9}O_2$@U6N, respectively.

2.3. Characterization of series samples

Morphologies, size and surface element distribution were analyzed by field emission scanning electron microscopy (FESEM, SU8020, Hitachi, Japan) and enlarged area were obtained through transmission electron microscope (TEM, Titan G2 ETEM, FEI, USA). Particle size was conducted from dynamic light scattering (DLS) conducted through a Zetasizer (Nano ZS, Malvern). Elemental species and surface chemical state was demonstrated through X-ray photoelectron spectroscopy (XPS, Escalab 2e50Xi, USA). The content of Ti and Zr in the samples was measured by an inductively coupled plasma optical emission spectrometer (ICP-OES) (Ultima2, HORIBA Joboin Yvon). The Langmuir and Branauer-Emmett-Teller (BET) specific surface area of resultant samples were measured and calculated using ASAP 2020 instrument, and the pore textural natures were calculated in density fractional function (DFT) model. The optical performances of the materials were studied by UV–vis diffuse reflectance spectra (DRS) equipped with the UV–vis spectrophotometer (UV2800, Tianjin Price Instrument Co., Ltd.), the region was set in 400 ~ 700 nm. Photoluminescence (PL) analysis was conducted on the fluorescence lifetime spectrophotometer (ZLX-PL-I, Beijing Zolix Co., Ltd.) to detect the generation of hydroxyl radicals adopting terephthalic acid (TA) as the probe molecule. A 300 W Xe lamp (CEL-HXF300-T3, AULTT, China) with a UV-cutoff filter as light source was put 12 cm over the liquid trap system. Electron spin resonance measurements (ESR) were performed at 77 K through an X-band ESR spectrometer (JEOL, Tokyo, Japan) and 5,5-dimethyl-1-pyrroline-N-oxide (DMPO) were the trapped agent. Electrochemical impedance spectroscopy (EIS) was adopted using a PARSTAT 4000+ electrochemical workstation with the excitation voltage was 5 mV and 6 M KOH was the electrolyte solution. Transient photocurrent responses were conducted in a quartz cell using 0.5 M Na_2SO_4 solution under various irradiation conditions (500 W Xe lamp, XD 350, China) and were recorded in the dark and under illumination.

2.4. Band gap measurement

To have a deeper understanding of optical performance in photocatalysis, the bandgap was conducted through the UV–vis diffuse reflectance spectra (DRS) and measured in the wavelength of 250 ~ 800 nm. The DRS data were evaluated according to the Kubelka-Munk function $F(R_\infty)$ from the Eqs. (1–3) [21], where

$$F(R_\infty) = \frac{(1-R_\infty)^2}{2R_\infty} \quad (1)$$

$$R_\infty = \frac{R_{\infty,\,sample}}{R_{\infty,\,reference}} \quad (2)$$

$$R_{\infty,\,reference} \approx 1 \quad (3)$$

The band gap was calculated by obtaining the intercept of the straight line in the linear area of $[F(R_\infty)hv]^{1/2}$ against hv, where hv expressed the energy of photon (eV).

2.5. Photocatalytic degradation measurements

In the typical reaction, UV–vis irradiation was implemented for the photocatalytic degradation of CH_3CHO (g) and the reaction process was conducted in a closed quartz glass jar micro-reactor (350 mL) under UV–vis motivation [1]. Primarily, 0.1 g of photocatalysts was deposited on the glass slide in the photocatalytic reactor and further sealed it. Then, the gaseous ALD (~ 1000 ppm) was injected into the apparatus and heated it in the oven for 3 min. Note that the sealed system was initially executed adsorption process in dark environment for 20 min with a RH of 75 %. Following by conducting the experiments under the excitation of UV–vis light source and the temperature was setting at 298 K through the double insulation system (Fig. S10). The concentration of ALD was detected through the gas chromatograph (GC, Agilent 7820 A). The degradation efficiency of gaseous ALD (η, %) was calculated using Eq. (4) [22]:

$$\eta\,(\%) = \frac{(C_0 - C)}{C_0} \times 100\% \quad (4)$$

Where C_0 and C represents for concentrations for the initial and remaining ALD, respectively.

2.6. Trapped experiments for reactive species identification

In the trapped experiments, 0.01 g of *p*-benzoquinone (PBQ), 2,2,6,6-tetramethyl-1-piperidinyloxy (TEMPO) and EDTA-2Na were mixed with 0.1 g photo-catalyst to quench the yielding superoxide radicals, hydroxyl radicals and irradiated holes, respectively. The samples were termed as "Scavenger: PBQ, Scavenger: TEMPO and Scavenger: EDTA-2Na", respectively.

3. Results and discussion

3.1. Scanning electron microscopy (SEM)

Figs. 1 and S1 integrated the SEM and TEM of as-synthesized samples. As exhibited in Fig. 1a, the PS microspheres modified by CTAB were highly uniform and homogeneous with an average diameter of about 335 nm, being consistent with that of unmodified counterpart (Fig. S1a). These CTAB modified PS microspheres afforded a multifunctional template for the preparation of hollow scaffold. Note that CTAB surfactant adopting in the procedure also featured a role of surface charge regulator, and effectively adjusted the surface potential of original PS from negative -41.26 mV (Fig. S1a) to positive 56.21 mV (Fig. 1a). This would be favorable for the subsequent electrostatic self-assembly with negatively charged particles [23]. As anticipated, H-$Zr_{0.1}Ti_{0.9}O_2$ (Fig. 1b) was well constructed on CTAB modified PS nanospheres, and it showed an average diameter of about 300 nm. The corresponding EDS mapping (Fig. S1b) of H-$Zr_{0.1}Ti_{0.9}O_2$ suggested the uniform distribution of Ti, O and Zr species.

Conversely, H-TiO_2 suffered a serious agglomeration in the absence of CTAB (Fig. S1c), while that was fully reversed for H-$Zr_{0.1}Ti_{0.9}O_2$ once CTAB surfactant was adopted (Fig. S1d). Notably, the outer texture of the H-TiO_2 (Fig. S1d) showed somewhat different morphology in comparison with the aforesaid H-$Zr_{0.1}Ti_{0.9}O_2$ (Fig. 1b). In the case of H-$Zr_{0.1}Ti_{0.9}O_2$, the surface appeared to be integrated and intact, while that of H-TiO_2 showed a coarse appearance. The differences further evidenced the fact that the metalation effect induced by *in situ* Zr-engineering could tailor nucleation and crystallization of crystals [24].

In order to construct a bistratal core-shell structure, ultrasmall UiO-66-NH_2 particles were successfully synthesized and grown on the surface of H-$Zr_{0.1}Ti_{0.9}O_2$. As clearly seen in Fig. S1e, the ultra-small UiO-66-NH_2 nanocrystals demonstrated the morphology of quasi-round shape with an average size of only ~ 36 nm, which was far less than the well-known UiO-66-NH_2 [25]. Thus, the resultant UiO-66-NH_2 nanocrystals were in favor of the uniform growth on the surface of H-$Zr_{0.1}Ti_{0.9}O_2$ layer. As expected, the morphologies of as-prepared H-$Zr_{0.1}Ti_{0.9}O_2$@U6N (Fig. 1c) were both intact and uniform, confirming the harmonious growth of UiO-66-NH_2 on the skeleton of H-$Zr_{0.1}Ti_{0.9}O_2$.

Besides, the TEM (Fig. 1d) along with EDS (Fig. 1e) mapping of H-

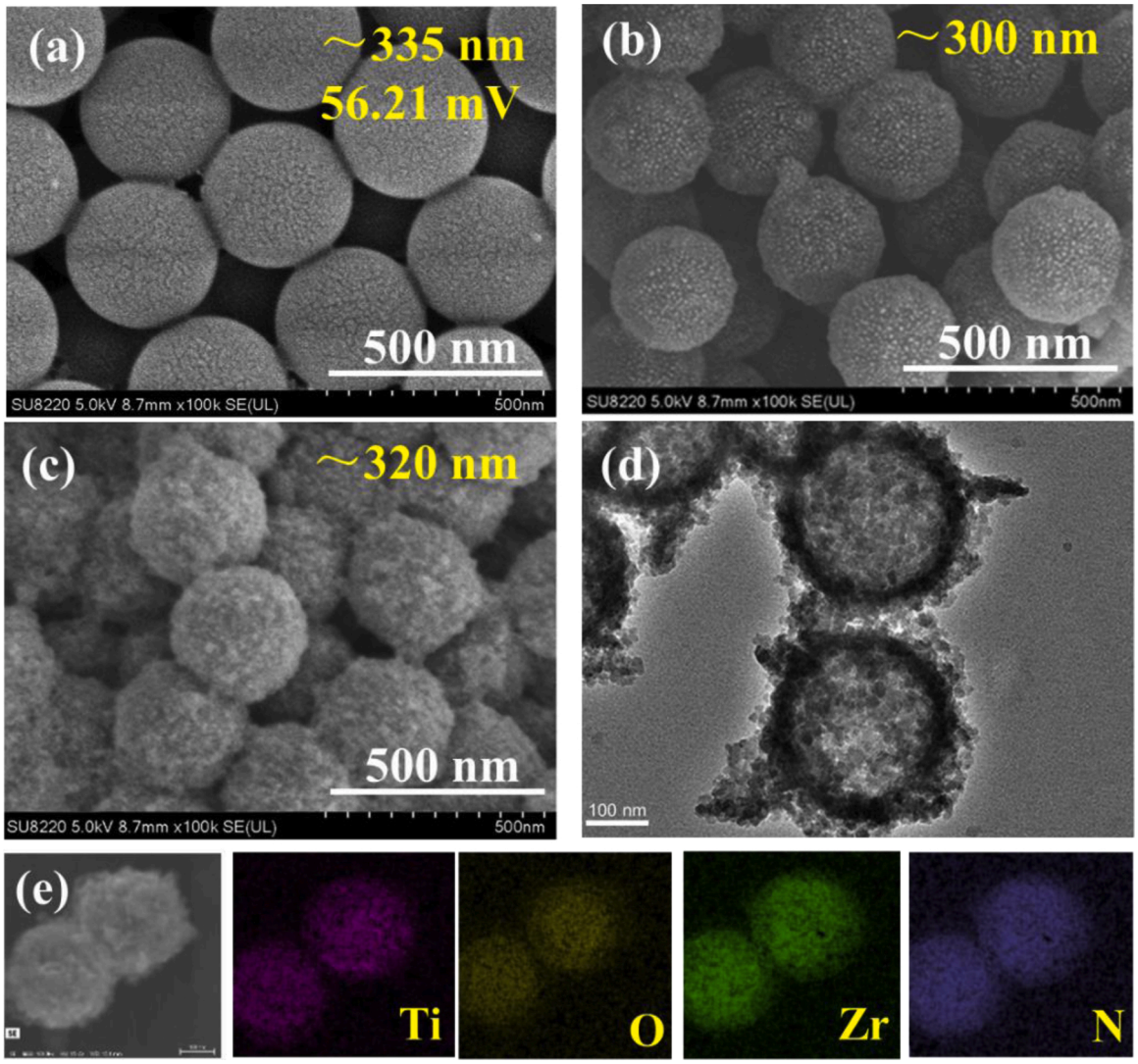

Fig. 1. SEM images of (a) modified PS microspheres, (b) H-Zr0.1Ti0.9O2, (c) H-Zr0.1Ti0.9O2@U6N, (d) TEM of H-Zr0.1Ti0.9O2@U6N, and (e) EDS mapping of Ti, O, Zr and N elements in H-Zr0.1Ti0.9O2@U6N.

$Zr_{0.1}Ti_{0.9}O_2$@U6N further confirmed the bistratal core-shell architecture with well-defined core-shell characters and intimate interface contact, suggesting the successful growth of UiO-66-NH_2 on the appearance of H-$Zr_{0.1}Ti_{0.9}O_2$. In contrast, UiO-66-NH_2 nanocrystals in H-TiO_2@U6N appeared to be somewhat scraggy and loosened on the surface of H-TiO_2 (Fig. S1f), reflecting the poor interface contact. By comparison, it was found that these UiO-66-NH_2 that grew on the surface of H-$Zr_{0.1}Ti_{0.9}O_2$ and H-TiO_2 presented distinct differences in MOF size, indicating that Zr engineering was crucial to the regulation of tailor-made MOF size and interface contact. It may be explained as following cases: (1) favorable coordination environment caused by Zr-engineered H-$Zr_{0.1}Ti_{0.9}O_2$ could preferably engineer the immobilization effect of native MOF ligands (termed as H_2BDC), and effectively attenuate the undesirable aggregation of second building units (SBU); (2) metalation effect derived from *in situ* Zr-engineering could induce greater electro-positivity and speed the nucleation behaviors of SBU [26,27]. Thus, it weakened the aggregation of SBU and favored the growth of uniform and ultra-small MOF nanocrystals.

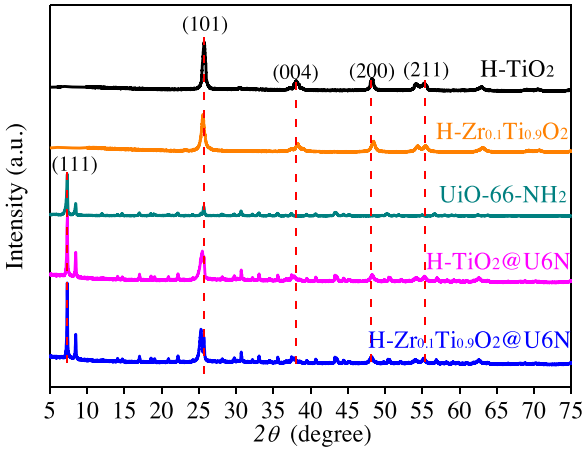

Fig. 2. PXRD pattern of H-TiO2, H-Zr0.1Ti0.9O2, UiO-66-NH2, H-TiO2@U6N and H-Zr0.1Ti0.9O2@U6N.

3.2. Structural characterizations

The crystallographic structure was characterized by PXRD method (Fig. 2). As can be seen, only anatase phase were detected [28,29] for H-TiO_2 and H-$Zr_{0.1}Ti_{0.9}O_2$. The peaks located at 25.7, 38.2, 48.4, and 55.5° could be ascribed to (101), (004), (200), (211) crystal facets of anatase TiO_2 (JCPDS 21-1272) [1,26], respectively. Moreover, no extra

peaks or impure crystalline phases (*e.g.* ZrO_2 and $ZrTiO_4$) were observed [26] for H-$Zr_{0.1}Ti_{0.9}O_2$, revealing that Zr element was just incorporated into the H-TiO_2 structure. The molar ratio (Zr/Ti), as determined by ICP-OES, was evaluated to be 9.8 % (Table S1), being consistent with the theoretical value. This result confirmed the successful implantation of Zr element in the structure of H-$Zr_{0.1}Ti_{0.9}O_2$. Interestingly, the (101) peak of Zr-engineered H-$Zr_{0.1}Ti_{0.9}O_2$ exhibited a slightly negative shift to lower diffraction angles compared with that of H-TiO_2 (Fig. S2), ascribing to the substitutional occupation of Zr^{4+} ions in the Ti^{4+} lattice [26]. Based on the dominant (101) facet, the average crystalline size of H-TiO_2 and H-$Zr_{0.1}Ti_{0.9}O_2$ could be calculated to be 12.7 and 10.2 nm (Table S2) by Scherrer equation [30]. The reduced crystal size suggested that Zr-engineering effectively tailored the crystal nucleation.

With respect to UiO-66-NH_2, it showed the similar diffraction peaks and agreed with the covered reports [31], demonstrating that the crystalline skeleton was well constructed [32]. As evidenced by the PXRD patterns of the H-TiO_2@U6N and H-$Zr_{0.1}Ti_{0.9}O_2$@U6N, the respective diffraction patterns for both components are observed, showing that the bistratal core-shell structure were both well crystallized with no extra species being detected. The estimated crystallite size of UiO-66-NH_2 according to (111) facet showed that the size of UiO-66-NH_2 in composited H-$Zr_{0.1}Ti_{0.9}O_2$@U6N appeared to be smaller than other two counterparts, exhibiting a sub-nanoscale measurement of 11.4 nm (Table S2).

To obtain information about the exact phase compositions and lattice parameters, PXRD patterns of the as-prepared materials were subjected to Rietveld structural refinements (Figs. S3–7 and Table S3) [36]. As shown, the simulated pattern after refinement matched well with the experimental data, and the difference curve only showed slight fluctuations, indicating that the simulated profiles were convinced. Through the refinements, Zr-bridged H-$Zr_{0.1}Ti_{0.9}O_2$ showed an intrinsic tetragonal structure with slight enhanced lattice parameters of $a = b$ =3.7701 Å and c =9.4318 Å in comparison with that of pristine H-TiO_2 ($a = b$ =3.7639 Å, c =9.4313 Å) (Table S3). The slight lattice expansion could be attributed to yielding Ti interstitial (Ti_i) defects, which was induced by Zr bridging [33,34]. For prepared UiO-66-NH_2, the refined cell parameters kept almost unchanged in compared to simulated UiO-66-NH_2 (Table S3). This further indicated that the structural geometry configurations of UiO-66-NH_2 remained unperturbed upon adopting the step-by-step assembly strategy.

By comparison, the refined parameters of H-TiO_2 ($a = b$ =3.7641 Å, c =9.4317 Å) and U6N ($a = b = c$ =20.7352 Å) in H-TiO_2@U6N (Tables S3) were found to be basically unchanged compared to the parent H-TiO_2 and UiO-66-NH_2, indicating an independent growth inclination at the interface for the two components. While for H-$Zr_{0.1}Ti_{0.9}O_2$ in H-$Zr_{0.1}Ti_{0.9}O_2$@U6N, the refined parameters of H-$Zr_{0.1}Ti_{0.9}O_2$ ($a = b$ =3.8190 Å, c =9.4518 Å) experienced an advanced lattice expansion (Table S3). The expansion in lattice parameters a, c and the cell volume for H-$Zr_{0.1}Ti_{0.9}O_2$ were likely due to the reason that the zirconium clusters with a larger ion radius in UiO-66-NH_2 penetrated into the lattice of H-$Zr_{0.1}Ti_{0.9}O_2$ through the forming interface contact [44]. Meanwhile, those of UiO-66-NH_2 in H-$Zr_{0.1}Ti_{0.9}O_2$@U6N exhibited reduced lattice parameters of $a = b = c$ =20.7018 Å (Table S3), attributing to the permeation of Ti clusters with smaller ion radius into the lattice of UiO-66-NH_2 [44]. Therefore, the bidirectional changes of lattice parameters only happened in the hybrid H-$Zr_{0.1}Ti_{0.9}O_2$@U6N suggested the formation of "Interfacial metal interpenetration" through the preferable interface contact.

3.3. N_2 adsorption and pore geometries analysis

To evaluate the geometrical porosities of as-prepared materials, N_2 adsorption isotherms of the as-synthesized materials were tested at 77 K (Fig. 3a), together with the structural parameters are integrated in Table 1. Obviously, both H-TiO_2 and H-$Zr_{0.1}Ti_{0.9}O_2$ exhibited very low surface area and eclipsed adsorption motivation. As expected, H-$Zr_{0.1}Ti_{0.9}O_2$ presented an elevated Brunauer-Emmett-Teller (BET) surface area of 103.9 m^2/g and a higher ratio of micropores (85.1 %) in comparison with that of H-TiO_2 (Table 1).

In case of U6N-based materials, we noticed that the N_2 adsorption capacity of composited H-TiO_2@U6N and H-$Zr_{0.1}Ti_{0.9}O_2$@U6N were declining compared to UiO-66-NH_2, mainly due to the reason that partial micropores in U6Ns were likely dominated by Ti phase. By comparison, H-$Zr_{0.1}Ti_{0.9}O_2$@U6N adsorbed N_2 with an apparent surface area of 1206.1 m^2/g and an estimated pore volume of 0.44 cm^3/g, both were higher than that of H-TiO_2@U6N (1003.3 m^2/g and 0.35 cm^3/g) (Table 1). The increased surface area and pore volume could be ascribed to the reduction in MOF size caused by "Interfacial metal interpenetration" of Zr/Ti clusters, as a result, improving the interface compatibility and weakening the diffusion barriers of probe molecules.

Fig. 3b explicated the pore size distribution (PSD) adopting the simulated density functional theory (DFT) model. Derived from the PSD analysis, highly intense characteristics peaks for H-TiO_2 were found at 16.0 and 22.7 Å, associating with the existence of mesoporous. Yet, there was one micropore peak with high intensity at about 14.6 Å for H-$Zr_{0.1}Ti_{0.9}O_2$, confirming the enhanced micropore configurations induced by Zr^{4+} engineering. For three U6Ns, one higher intense peak centered at 6.40 ~ 6.50 Å emerged (inset in Fig. 3b), corresponding to the emblematic aperture of U6N, being accordant with covered reports [35]. Note that the peak intensity H-$Zr_{0.1}Ti_{0.9}O_2$@U6N located at 6.4 Å appeared to be somewhat higher than that of H-TiO_2@U6N, indicating that UiO-66-NH_2 grew well on the surface of H-$Zr_{0.1}Ti_{0.9}O_2$ and enabled

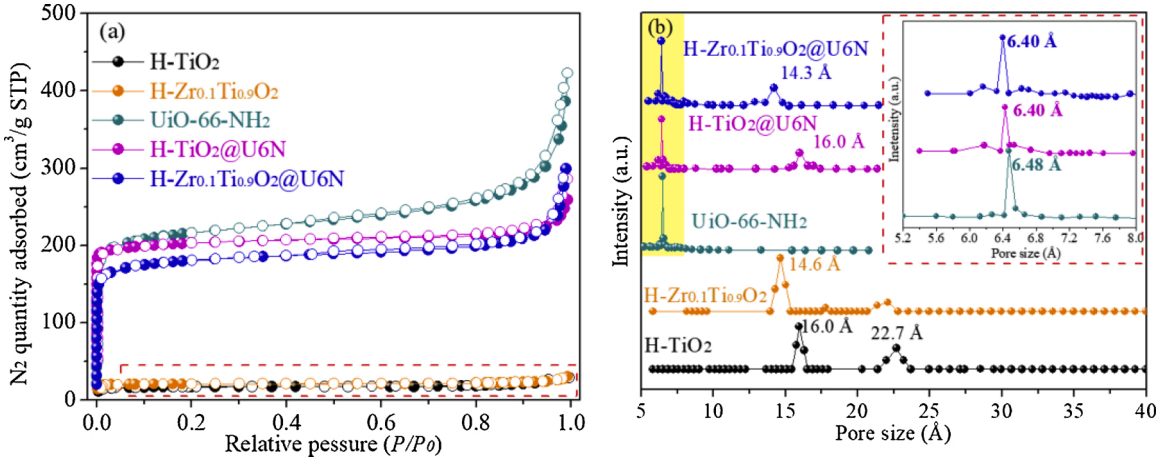

Fig. 3. (a) N2 adsorption of as-synthesized samples and (b) pore size distribution using DFT model.

Table 1
Textural parameters of as-synthesized samples.

Sample	S_{BET}[a] (m^2/g)	S_{micro}[b] (m^2/g)	S_{micro}/ S_{bet} (%)	V_t[c] (cm^3/g)	V_{micro}[d] (cm^3/g)	V_{micro}/V_t (%)
H-TiO_2	74.1	44.8	60.5	0.21	0.15	71.4
H-$Zr_{0.1}Ti_{0.9}O_2$	103.9	88.4	85.1	0.23	0.19	82.6
UiO-66-NH_2	1398.9	1347.1	96.3	0.52	0.49	94.2
H-TiO_2@U6N	1003.3	763.5	76.1	0.35	0.29	84.0
H-$Zr_{0.1}Ti_{0.9}O_2$@U6N	**1206.1**	**1087.9**	**90.2**	**0.44**	**0.40**	**90.3**

[a] S_{BET} is the surface area of BET.
[b] S_{micro} is the surface area of microporous structure.
[c] V_t is the total volume.
[d] V_{micro} is microporous volume.

a favorable interface contact. Additionally, one extra peak concentrated at 14.3 and 16.0 Å was also probed for H-$Zr_{0.1}Ti_{0.9}O_2$@U6N and H-TiO_2@U6N, respectively, inheriting the intrinsic pore natures of H-$Zr_{0.1}Ti_{0.9}O_2$ and H-TiO_2. As a consequence, the interconnected double apertures would facilitate the synergetic adsorption in favor of mass transfer of reactants and products.

3.4. X-ray photoelectron spectroscopy (XPS) analysis

XPS analysis was employed to investigate the chemical state and composition. Full survey spectra of these synthesized samples shown in Fig. S9a verify the existence of Zr, N, Ti and O elements. Fig. 4a showed Ti 2p core level peaks of H-TiO_2, H-$Zr_{0.1}Ti_{0.9}O_2$, H-TiO_2@U6N and H-$Zr_{0.1}Ti_{0.9}O_2$@U6N. As plotted in Fig. 4a, Ti 2p peaks of H-TiO_2 at the binding energy (BE) of 458.54 and 464.37 eV were indicative of Ti^{4+} $2p_{3/2}$ and Ti^{4+} $2p_{1/2}$. These two peaks showed a slight negative shift in H-$Zr_{0.1}Ti_{0.9}O_2$ (458.43 and 464.29 eV) for Zr-bridged H-$Zr_{0.1}Ti_{0.9}O_2$, attributing to generate geometrical defects [36]. It is well perceived that the shift of BE was indicative of strong interfacial interaction and charge migration. As seen from H-TiO_2@U6N, BE value of Ti 2p (458.51 and 464.34 eV) did not change obviously in comparison with that of H-TiO_2 (458.54 and 464.37 eV), foreboding a negligible change and electron migration in the interface. Whereas, in case of H-$Zr_{0.1}Ti_{0.9}O_2$@U6N, an obvious negative shift of Ti 2p (458.34 and 464.22 eV) relative to H-TiO_2 (Fig. 4a) was observed. Such shift could be ascribed to the metal interpenetration of zirconium into the lattice of H-$Zr_{0.1}Ti_{0.9}O_2$, as a result, weakening the coordination environment of Ti species. Meanwhile, two deconvoluted peaks centered at about 457.72 (Ti^{3+} $2p_{3/2}$-N) and 462.75 eV (Ti^{3+} $2p_{1/2}$-N) emerged. The formation of Ti^{3+} species were due to the accumulation of transferred electrons in Ti^{4+} site, resulting in the reduction of Ti^{4+} [37]. Hereby, it could be reasonably deemed that there being a well-organized interface alignment between H-$Zr_{0.1}Ti_{0.9}O_2$ and UiO-66-NH_2, enabling an electron transfer from UiO-66-NH_2 to H-$Zr_{0.1}Ti_{0.9}O_2$. Besides, high resolution of Zr 3d XPS was further determined to explore the metal interpenetration. As observed in Fig. S9b, both Zr-O species in H-TiO_2@U6N remained unchanged compared to that of pristine U6N, yet that exhibited negative shift for H-$Zr_{0.1}Ti_{0.9}O_2$@U6N, suggesting weakened coordination environment of Zr species. These changes in coordination environment of Zr were caused by the doping of Ti into the lattice of Zr, affording crucial evidence to verify the proposed "Interfacial metal interpenetration".

In order to probe the transfer behaviors, high resolution of N 1s and O 1s core levels were further measured. As seen from Fig. 4b, N 1s peaks of UiO-66-NH_2 at BE of 398.26 and 399.11 eV were indicative of N—C and N—H bonds in the ligands [38]. For H-TiO_2@U6N, it exhibited almost unchanged BE for N—C (398.30 eV) and N—H (399.10 eV) bonds, reflecting the transfer barriers in the electron migration process. Whereas, the two peaks of H-$Zr_{0.1}Ti_{0.9}O_2$@U6N shifted to higher BE of 398.42 and 399.57 eV compared to UiO-66-NH_2 and H-TiO_2@U6N (Fig. 4b), implying that a largely electron cloud density in -NH_2 groups migrated from UiO-66-NH_2 to H-$Zr_{0.1}Ti_{0.9}O_2$ [32]. Besides, an emerging peak located at 401.30 eV could be observed (Fig. 4b), corresponding to N-Ti^{3+} bonding [3]. Combined with the analysis of Ti 2p, it could be concluded that the electron density could directly migrate from the -NH_2 groups in UiO-66-NH_2 to Ti sites in H-$Zr_{0.1}Ti_{0.9}O_2$. The migration path would positively overcome transmission jam of photo-induced electron

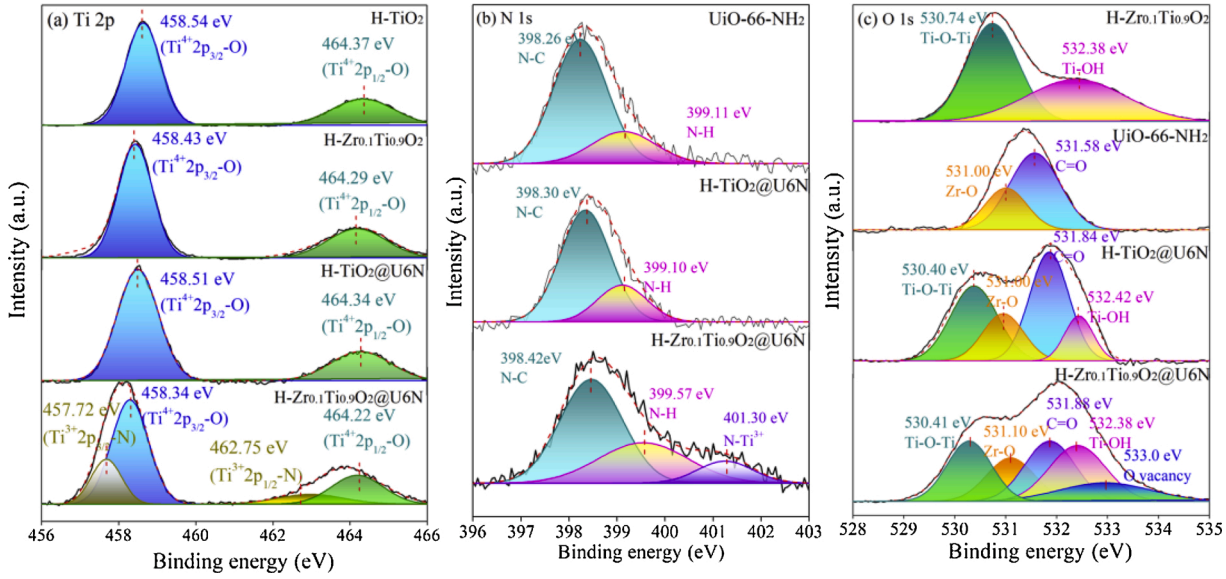

Fig. 4. High resolution XPS of (a) Ti 2p in H-TiO2, H-Zr0.1Ti0.9O2, H-TiO2@U6N and H-Zr0.1Ti0.9O2@U6N; (b) N 1s in UiO-66-NH2, H-TiO2@U6N and H-Zr0.1Ti0.9O2@U6N; (c) O 1s in H-Zr0.1Ti0.9O2, UiO-66-NH2, H-TiO2@U6N and H-Zr0.1Ti0.9O2@U6N.

and advance the separation efficiency of photogenerated carriers.

Additionally, O 1s spectra were further explored to unravel the migration path of charges (Figs. 4c and Fig. S9c). As observed, the high-resolution spectra of O 1s in H-TiO_2 (Fig. S9c) showed an asymmetric profile, which corresponded to two different oxygen species in H-TiO_2. The two peaks at 530.87 eV (Ti-O-Ti) and 532.38 eV (Ti−OH) were assigned to lattice oxygen and chemisorbed oxygen species (*e.g.* hydroxyl species) [39]. Furthermore, Zr bridging in H-$Zr_{0.1}Ti_{0.9}O_2$ showed a negative shift (530.74 eV) of Ti-O-Ti bonding (Fig. 4c) compared to that of H-TiO_2 (530.87 eV), indicating that implanted Zr had embedded into the lattice of H-$Zr_{0.1}Ti_{0.9}O_2$ and weaken the coordination environments of Ti-O-Ti bonding [40]. Another point should be noted that the peak area ratio of Ti−OH species in H-$Zr_{0.1}Ti_{0.9}O_2$ was calculated to be accounting for 45 %, higher than that of H-TiO_2 (30 %) (Table S4). Such enhancement of hydroxy specie was due to the case that Zr-bridging strategy was conducive to the surface hydroxylation for H-$Zr_{0.1}Ti_{0.9}O_2$, and this was an important factor in the following photo-catalytic process. For UiO-66-NH_2, it showed typical peaks at 531.00 and 531.58 eV, assigning to the BE of Zr-O and C═O species in SBU [41], respectively. While for H-$Zr_{0.1}Ti_{0.9}O_2$@U6N, the O 1s peak could be fitted into five peaks, unambiguously inheriting the respective traits of single-component UiO-66-NH_2 and H-$Zr_{0.1}Ti_{0.9}O_2$. After a careful examination of BEs, it was observed that of Zr-O (531.10 eV) and C═O (531.88 eV) species in H-$Zr_{0.1}Ti_{0.9}O_2$@U6N shifted positively by 0.1 and 0.3 eV compared to pristine UiO-66-NH_2 (531.00 and 531.58 eV), indicating the electron transferred from Zr-O and C═O species in SBU to H-$Zr_{0.1}Ti_{0.9}O_2$. Yet, with regard to H-TiO_2@U6N, only one peak associating with C═O species (531.84 eV) was responsible for a positive shift (by 0.26 eV) compared to that of UiO-66-NH_2, reflecting the impeditive migration process for photoinduced electrons [42]. In other words, Zr bridging could profitably customize the geometric and electronic features of H-$Zr_{0.1}Ti_{0.9}O_2$, so that a matched band alignment and stronger heterojunction interface could be constructed between H-$Zr_{0.1}Ti_{0.9}O_2$ and UiO-66-NH_2. Such results could be further verified by Ti-O-Ti bonding. As explicitly expounded in Fig. 4c, the Ti-O-Ti species in H-$Zr_{0.1}Ti_{0.9}O_2$@U6N exhibited a reduced BE of 530.41 eV compared to that of H-$Zr_{0.1}Ti_{0.9}O_2$ (530.74 eV), confirming an increased electron density of Ti-O-Ti due to intimate interface interaction. Therefore, for H-$Zr_{0.1}Ti_{0.9}O_2$@U6N, the enrichment of electrons in Ti-O-Ti species echoed well with the decreased electrons of SBU, effectively driving the reduction process of Ti^{4+} and propelling the formation of Ti^{3+} species (Fig. 4a). Besides, an additional peak concentrated at 533.00 eV corresponded to the adsorbed oxygenous species in the vicinity of oxygen vacancies (O_v). Notably, the peak area ratio of Ti−OH in H-$Zr_{0.1}Ti_{0.9}O_2$@U6N was calculated to be 26.3 %, obviously higher than that of H-TiO_2@U6N (15.2 %) (Table S5). This attributed to the tiny penetration of Ti clusters in the lattice of UiO-66-NH_2 through the interface, and formed coordination with free carboxyl groups in MOF, as a consequence, contributing to the increased Ti−OH species. Combined with the analysis of XRD refinements, we reasoned that Zr bridging could be favorable for the bidirectional penetration of Zr and Ti clusters in the interface. This unique bidirectional penetration of Ti-Zr in both crystal lattices would be expected to improve the interface compatibility for UiO-66-NH_2 and H-$Zr_{0.1}Ti_{0.9}O_2$, and overcome transmission jam of photo-induced electron as well as shortened the "adsorption-catalysis" pathway.

3.5. Photocatalytic degradation activity for vaporous ALD

A model photo-catalytic reaction of gaseous ALD was executed to conduct the photo-catalytic activity of the photo-catalysts under 75 RH %. To be noted, the adsorption behavior was preferentially conducted in the dark to test the function of surface adsorption on the photocatalytic activity and shown in Fig. S11a. As shown, the adsorption equilibrium of ALD over the samples could be accomplished within 20 min and the adsorption performance was up to 20 % for H-$Zr_{0.1}Ti_{0.9}O_2$@U6N, higher than that of pure UiO-66-NH_2 (14 %) despite having higher surface area (1398.9 m^2/g). In addition, the adsorption rates of these samples were estimated and shown in Fig. S11b. It reflected that H-$Zr_{0.1}Ti_{0.9}O_2$@U6N possessed the highest k_a value of 0.020 min^{-1}, about 20 times as high as that of benchmark H-TiO_2 (0.001 min^{-1}) and 6.7 times of H-$Zr_{0.1}Ti_{0.9}O_2$ (0.003 min^{-1}), exhibiting a significant enhancement on adsorption ability towards ALD. The improved adsorption actions may be attributed to generated Ti^{3+} defects and O vacancies in H-$Zr_{0.1}Ti_{0.9}O_2$ would enhance the surface polarization, effectively exerting a synergistic adsorption of polar ALD [43,44]. Moreover, the internal hollow merits could facilitate the mass transfer and strength adsorption driving force for ALD molecule, as a result, cooperatively contributing to elevated adsorption rates.

Fig. 5a shows the detailed degradation profiles of CH_3CHO over different samples upon the vis-light irradiation with a RH of 75 %. Evidently, the degradation efficiency of H-$Zr_{0.1}Ti_{0.9}O_2$ increased by 20 % compared to H-TiO_2 (12 %), attributing to the formation of active lattice defects in H-$Zr_{0.1}Ti_{0.9}O_2$, which effectively boost the photocatalytic activity [45]. For pure UiO-66-NH_2, it exhibited an elevated 60 % photo-catalytic activity, about 30 % higher than that of H-$Zr_{0.1}Ti_{0.9}O_2$. This could be due to the photosensitivity of NH_2 motifs in the structure of MOFs, extending the light-response to visible region in comparison to H-$Zr_{0.1}Ti_{0.9}O_2$ and pristine H-TiO_2 [2]. Excitingly, the photocatalytic activity was conspicuously advanced once integrated the bilateral strengths of both H-$Zr_{0.1}Ti_{0.9}O_2$ and UiO-66-NH_2. As expected, H-$Zr_{0.1}Ti_{0.9}O_2$@U6N ranked at the top of photo-activity, with 98 % of ALD being decomposed after only 20 min (Fig. 5a) under similar test conditions, which also exceeded that of H-TiO_2@U6N (80 %). The excellent degradation activity of H-$Zr_{0.1}Ti_{0.9}O_2$@U6N could be traced to following factors: (1) outstanding synergistic adsorption behaviors of ALD and generated active sites *i.e.* Ti^{3+} (or/and O vacancies) in H-$Zr_{0.1}Ti_{0.9}O_2$, resulting in the enhanced degradation; (2) the improved interface alignment and compatibility upon Zr/Ti penetration shortened the transmission path of electrons and advanced the separation efficiency photoinduced carriers [46].

Furthermore, pseudo-first order model was adopted to explore the kinetics behavior of CH_3CHO photocatalytic process using Eq. (5) [2]:

$$\ln\frac{C}{C_0} = kt \tag{5}$$

C/C_0 is the normalized concentration of CH_3CHO, k reflects the apparent reaction rate constant (min^{-1}), and t is reaction time (min).

As shown in Fig. 5b, photocatalytic degradation profiles matched well with pseudo-first order equation ($R^2 > 0.99$). The fitting rate constant of H-$Zr_{0.1}Ti_{0.9}O_2$@U6N reached up to 0.195 min^{-1}, which were 97.5, 32.5, 13.9 and 5.1 folds enhancement than that of H-TiO_2 (0.002 min^{-1}), H-$Zr_{0.1}Ti_{0.9}O_2$ (0.006 min^{-1}), UiO-66-NH_2 (0.014 min^{-1}) and H-TiO_2@U6N (0.038 min^{-1}), respectively. Results showed that the combination of H-$Zr_{0.1}Ti_{0.9}O_2$ and UiO-66-NH_2 could effectively enhance the photo-degradation kinetics by orders of magnitude. The superior photoactivity of H-$Zr_{0.1}Ti_{0.9}O_2$@U6N over other materials was likely due to the obvious charge separation resulting from the bidirectional penetrated interface, the enhanced visible photoactivity induced by the NH_2 moieties, as well as emerging Ti defects and O vacancies in H-$Zr_{0.1}Ti_{0.9}O_2$. In order to investigate the defects in photocatalysts, CO-DRIFS spectra analysis was further determined. As shown in Fig. 5c, it showed the CO-DRIFS patterns on selected H-TiO_2, H-$Zr_{0.1}Ti_{0.9}O_2$ and H-$Zr_{0.1}Ti_{0.9}O_2$@U6N. Clearly, all the samples exhibited undiminished bands at 2173 and 2114 cm^{-1} under three temperatures, mainly crediting to the chemisorbed CO molecule. Note that the peak intensity of H-TiO_2 and H-$Zr_{0.1}Ti_{0.9}O_2$ decreased as the temperature increased, while that of H-$Zr_{0.1}Ti_{0.9}O_2$@U6N remained unchanged, suggesting the improved Lewis acidity [47]. The enhanced surface Lewis acidity would customize the surface polarization of H-$Zr_{0.1}Ti_{0.9}O_2$ [53], boosting the adsorption of polar ALD molecule [54].

In order to probe the influence of relative humidity on the

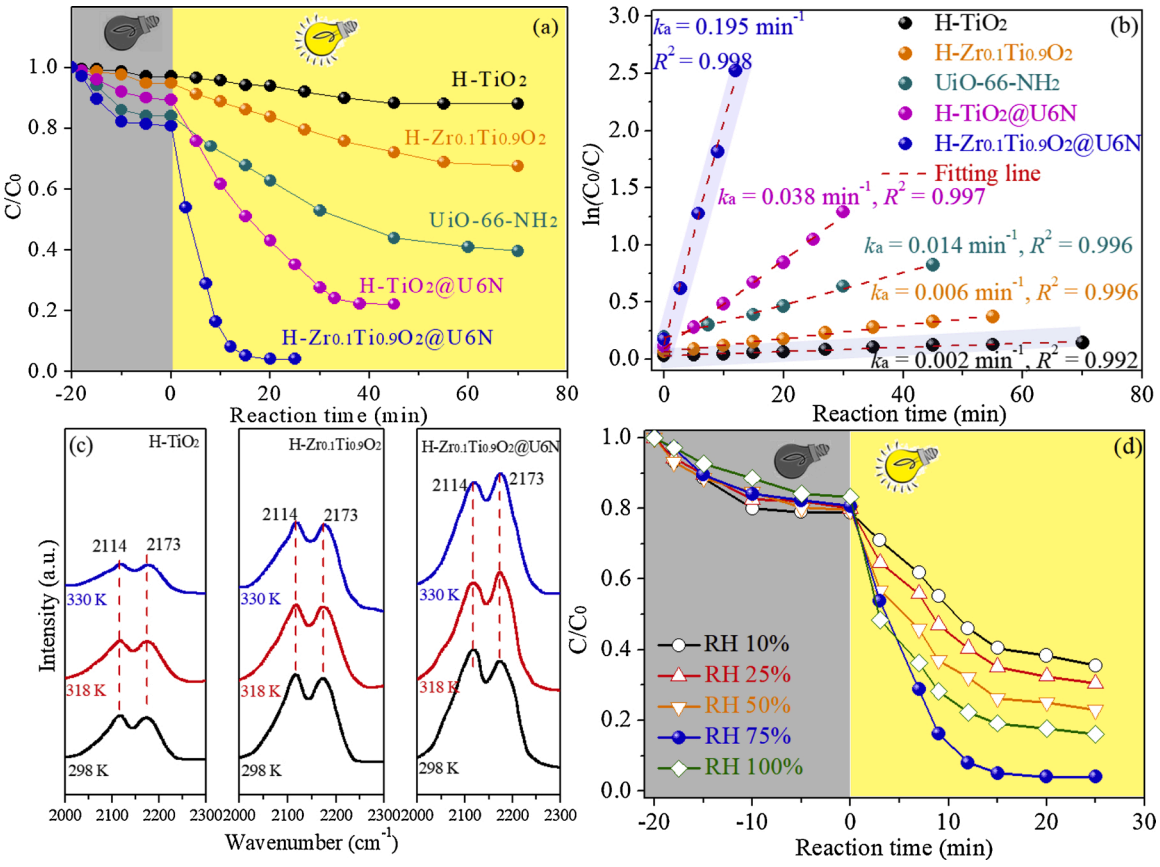

Fig. 5. (a) Photocatalytic degradation rate, (b) pseudo-first-order kinetics curves of photocatalytic degradation, (c) CO-DRIFS spectra of H-TiO2, H-Zr0.1Ti0.9O2, H-Zr0.1Ti0.9O2@U6N and (d) Photocatalytic degradation rate of H-Zr0.1Ti0.9O2@U6N under different RH values.

photocatalytic performance, we further executed the photocatalytic tests under different relative humilities (RH) (10 ~ 100 %). As can be seen in Fig. 5d, when the relative humidity increased from 10 ~ 75 %, the photocatalytic properties of H-$Zr_{0.1}Ti_{0.9}O_2$@U6N was obviously advanced, having an increase of photocatalytic activity from 65 % to 98 % within about 25 min reaction. Obviously, relative humidity exerted a promotional effect on the photocatalytic reaction. After that, a slight declining of its photocatalytic activity (84 %) was observed as the humidity rose to 100 %. As calculated, the evaluated degradation rate of H-$Zr_{0.1}Ti_{0.9}O_2$@U6N followed the orders: 0.195 min^{-1} (75 RH%) > 0.106 min^{-1} (100 RH%) > 0.071 min^{-1} (50 RH%) > 0.055 min^{-1} (25 RH%) > 0.045 min^{-1} (10 RH%) (Fig. S11c). Hence, the presence of water could facilitate to produce more surface hydroxyl groups to some extent, which would be helpful for the oxidation of ALD. However, the excess vaporous water would form competitive adsorption with ALD on H-$Zr_{0.1}Ti_{0.9}O_2$@U6N, which cannot be transformed into ·OH radicals in time and thus weakened the photocatalytic activity.

For comparison, the photo-catalytic degradation of ALD over various state-of-the-art photo-catalysts under vis-light irradiation were observed in Fig. S11d (Detailed information see Table 2). By comparison, there may exist a called "trade-off" effect between photo-activity and degradation rate constant over most samples. Namely, higher photo-activity and excellent kinetic rates were not always synchronous [48,49]. Additionally, it was well established that kinetic behavior was associated with the mass transfer of guest molecules [50,51], reflecting its diffusion motivation in the materials. Taking an example of rGO-TiO_2, it elucidated an outperforming photo-catalytic activity of 96 % for ALD degradation under similar conditions, yet it exhibited an eclipsed kinetic rate of 106 × 10^{-3} min^{-1} (Table 2) [52], which reflected somewhat obstructive for ALD diffusion. Conversely, for the custom-designed H-$Zr_{0.1}Ti_{0.9}O_2$@U6N, it revealed the quasi-perfect photoactivity within 20 min but record-high degradation rate constant (195 × 10^{-3} min^{-1}) to our knowledge, almost 98 and 16-folds enhancement in comparison with H-TiO_2 (0.002 min^{-1}) and Ag@TiO_2 (11.9 × 10^{-3} min^{-1}) competitors (Table 2), respectively. The excellent kinetic behavior for H-$Zr_{0.1}Ti_{0.9}O_2$@U6N were mainly attributed to: (1) the intrinsic hollow structure of H-$Zr_{0.1}Ti_{0.9}O_2$ could exert a positive effect for the mass transfer of ALD and the emission of products; and (2) the penetrated interface between H-$Zr_{0.1}Ti_{0.9}O_2$ and UiO-66-NH_2 could form intimate heterostructure and expedited the separation of photo-induced carriers.

Table 2
Photocatalytic performance for the photocatalytic degradation of ALD over various state-of-the-art photocatalysts under vis-light irradiation.

Catalysts	ALD concentration (ppm)	Dosage (g)	Photocatalytic activity (%)	Kinetic rate (10^{-3} min^{-1})	Ref.
H-$Zr_{0.1}Ti_{0.9}O_2$@U6N	**500**	**0.1**	**98**	**195**	**This work**
H-TiO_2	**500**	**0.1**	**12**	**2**	**This work**
ZnO-rGO	200	0.2	96	8.1	[70]
rGO-TiO_2	25	0.1	96	106	[71]
Ag@TiO_2	500	0.2	72	11.9	[72]
Melam/WO_3	150	0.5	95	11.5	[73]
Rh/Sb-$SrTiO_3$	150	0.3	95	22	[74]

Therefore, the synchronous advancements of photoactivity and kinetic rate for H-$Zr_{0.1}Ti_{0.9}O_2$@U6N efficaciously overcame the "trade-off" barrier, affording a new benchmark in exploring novel photocatalysts.

In addition to the photocatalytic efficiency, the stability of the photocatalyst we designed for recycling is also a key issue to evaluate the quality of the materials. Hence, the stability of the best-performing H-$Zr_{0.1}Ti_{0.9}O_2$@U6N was evaluated by repeatedly photodegrading ALD under the same conditions. As seen in Fig. S12a, it showed only a 4% drop in the degradation efficiency of ALD degradation after six cycles, suggesting an excellent stability and durability. SEM and XRD patterns of H-$Zr_{0.1}Ti_{0.9}O_2$@U6N in Fig. S12b-c after sixth cycles demonstrated that the surface morphology and crystal structure maintained well after the recycling reaction. Besides, N_2 adsorption test of H-$Zr_{0.1}Ti_{0.9}O_2$@U6N yielded a quasi-invariable value of 1187.2 m^2/g (Fig. S12d), suggesting an inherited surface area. Consequently, the above results showed higher photo-catalytic activity, stability and durability. It makes H-$Zr_{0.1}Ti_{0.9}O_2$@U6N a broad application prospect in environmental restoration and sustainable energy transformation.

3.6. UV–vis DRS, interface charges transfer and separation analysis

UV–vis DRS, as shown in Fig. 6a–b, were used to probe the optical performance of photo-catalysts. Obviously, H-TiO_2 exhibited a threshold in the UV response at ~ 390 nm, while it expanded toward visible region (~ 410 nm) for H-$Zr_{0.1}Ti_{0.9}O_2$. This was due to the generated defect sites in H-$Zr_{0.1}Ti_{0.9}O_2$ caused by Zr^{4+} engineering that extended and promoted the light adsorption [53]. For pure UiO-66-NH_2, it exhibited the visible-light adsorption edges at ~ 430 nm, owing to the absorption of NH_2 functional motifs. Specially, the fabricated H-$Zr_{0.1}Ti_{0.9}O_2$@U6N integrated and inherited the bilateral superiorities of H-$Zr_{0.1}Ti_{0.9}O_2$ and UiO-66-NH_2, exhibiting an obvious red shift of adsorption edge and advanced absorption strength in visible-light area ($\lambda > 490$ nm) compared to other competitors. Besides, Fig. 6b showed the plots obtained *via* the transformation based on the Kubelka-Munk function. Noticeably, H-$Zr_{0.1}Ti_{0.9}O_2$ displayed reduced band gap (E_{bg}) (3.00 eV) compared to that of H-TiO_2 (3.20 eV), mainly attributing to the introduction of defect levels after Zr^{4+} doping that contributed to the upshift of valance band (VB) and narrowed the E_{bg} [54]. For H-$Zr_{0.1}Ti_{0.9}O_2$@U6N, it exhibited the lowest E_{bg} of 2.32 eV, lower than that of UiO-66-NH_2 (2.68 eV) and H-TiO_2@U6N (2.60 eV). The E_{bg} reduction of H-$Zr_{0.1}Ti_{0.9}O_2$@U6N was assigned to the formation of Ti^{3+} defects in H-$Zr_{0.1}Ti_{0.9}O_2$, which narrowed the band gap [55].

The PL analysis in Fig. 6c was used to investigate the interface charges transfer and separation. As seen, a magnificent band with highest intensity was observed for benchmark H-TiO_2, implying the worst recombination of generated electron-hole pairs. Delightedly, the PL was sharply declined with respect to H-$Zr_{0.1}Ti_{0.9}O_2$. This was credited to the generation of oxygen vacancies, and positively facilitated the mobility of photo-generated charge carriers and improved their separation. For H-$Zr_{0.1}Ti_{0.9}O_2$@U6N, it exhibited barely PL intensity than that of UiO-66-NH_2 and H-TiO_2@U6N, confirming that the bidirectional penetrated interface could effectively suppress the charge recombination and elongate the lifetime of charge carriers. Besides, defect-related levels in the band gap induced by oxygen vacancies could serve as sinks to cooperatively trap the excited carriers and retarded the recombination [56,57]. More specially, the improved compatible interface between H-$Zr_{0.1}Ti_{0.9}O_2$ and UiO-66-NH_2 efficiently overcame transmission barriers of electrons.

Moreover, electrochemical impedance spectroscopy (EIS) in Fig. 6d was recorded to investigate the separation efficiency of carriers. In the EIS Nyquist plots, the smaller semicircle size suggested an effective separation of generated electron-hole pairs and fast interfacial charge transfer [29]. Obviously, the impedance arc radius of H-$Zr_{0.1}Ti_{0.9}O_2$@U6N was the smallest as compared to other samples, implying rapid migration of photo-generated electron-hole pairs and effective separation. It has been covered that the Ti^{3+}-related defects in H-$Zr_{0.1}Ti_{0.9}O_2$ could help to afford more active sites and decrease the transport resistance of photo-generated electrons, allowing swift transmission efficiency [1,3]. Moreover, the bidirectional penetrated interface would be favorable to overcome the transmission barriers of photo-induced electrons. The aforementioned results were well consistent with our PL analysis, and clearly validated the importance of structuring synergetic interface hetero-junction and effectively advanced the separation of photo-generated electron-hole pairs.

The satisfied separation efficiency of carriers was further verified *via* the surface photovoltage spectroscope (SPS) (Fig. 6e). Generally, it is widely accepted that the intensity of SPS peak mainly depends on the concentration of molecule oxygen, reflecting the separation of the photogenerated charges [58,59]. As shown in Fig. 6e, an enhanced SPS response corresponding to higher separation of carriers was observed for

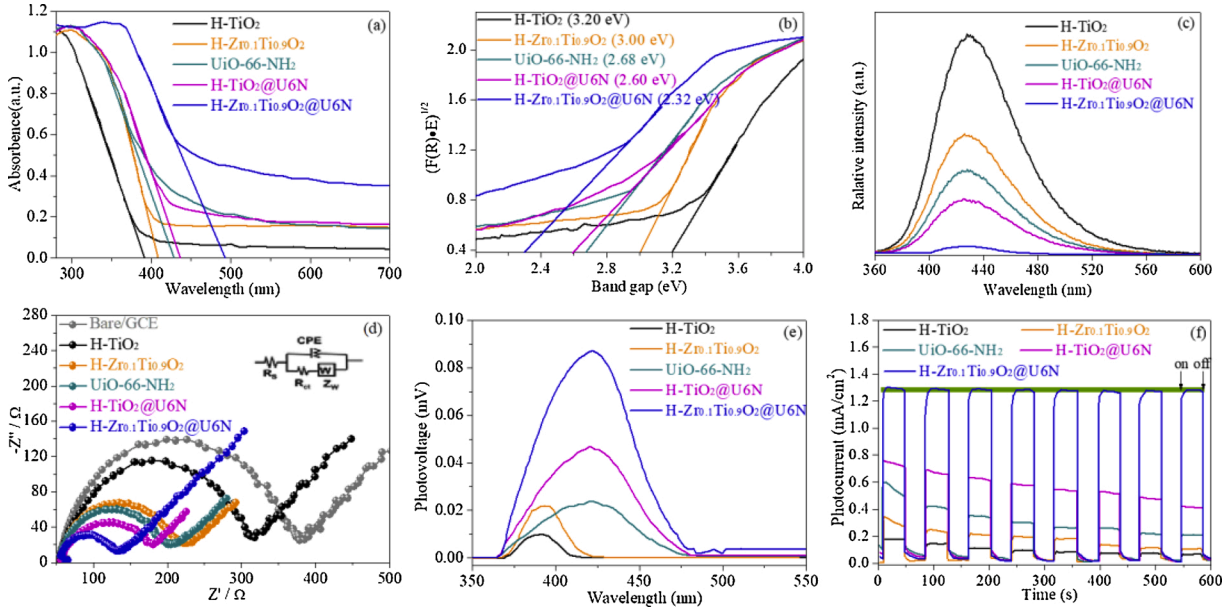

Fig. 6. (a) UV–vis DRS, (b) plots of transformed Kubelka-Munk function *vs.* photon energy of as-prepared samples, (c) PL emission spectra, (d) electrochemical impedance spectroscopy, (e) photovoltage spectroscope response analysis and (f) photocurrent responses under vis-light irradiation.

H-$Zr_{0.1}Ti_{0.9}O_2$. This enhancement confirmed that the generated defects sites in H-$Zr_{0.1}Ti_{0.9}O_2$ structure would be beneficial to boost the adsorption of oxygen molecules and effectively capture the photo-generated electrons. Expectedly, H-$Zr_{0.1}Ti_{0.9}O_2$@U6N with tight interface contact exhibited strongest SPS response after coupling with UiO-66-NH_2 nanocrystals, suggesting the efficient separation of the photogenerated charges.

Photocurrent measurements were subsequently performed to evaluate the charge transfer and separation behaviors. As shown in Fig. 6f, the photocurrent density increased sharply when the light was switched on, and immediately returned to its initial negligible value after the light source was turned off. It is well established that the photocurrent is stimulated by diffusion electrons from the separation of the electron-hole pairs induced by visible light [60]. Expectedly, H-$Zr_{0.1}Ti_{0.9}O_2$@U6N displayed the highest photocurrent response and kept almost identical after eight cycles, suggesting that H-$Zr_{0.1}Ti_{0.9}O_2$@U6N possessed marked driving force in producing and transferring the photoexcited charge carrier under UV–vis light stimulation. While for other materials, the absence of interface heterojunction or poor interface compatibility would greatly weaken the separation efficiency of charges. These results, in combination with above-mentioned analysis, further confirmed the importance of bidirectional penetrated interface in H-$Zr_{0.1}Ti_{0.9}O_2$@U6N for overcoming the transmission jam of photo-induced charges.

3.7. *Investigation of charges separation adopting in situ Kelvin probe force microscopy*

In situ Kelvin probe force microscopy (KPFM) was known as an evaluable and valid method to investigate the separation efficiency of photo-induced carriers [4]. The images of atomic force microscopy (AFM) together with corresponding line profiles of the surface photovoltage (SPV) on selected H-$Zr_{0.1}Ti_{0.9}O_2$, UiO-66-NH_2 H-$Zr_{0.1}Ti_{0.9}O_2$@U6N and were shown in Fig. 7. As shown in Fig. 7a, 7d and 7 g, they showed the nano-particle of these selected H-$Zr_{0.1}Ti_{0.9}O_2$, UiO-66-NH_2, H-$Zr_{0.1}Ti_{0.9}O_2$@U6N, which was executed to probe the changes in SPV signals during the irradiation process. As observed in Fig. 7b and 7e, both H-$Zr_{0.1}Ti_{0.9}O_2$ and UiO-66-NH_2 reflected slight changes in SPV signals, indicating the obstructive process for the migration of irradiated electrons [4]. Yet, in the case of

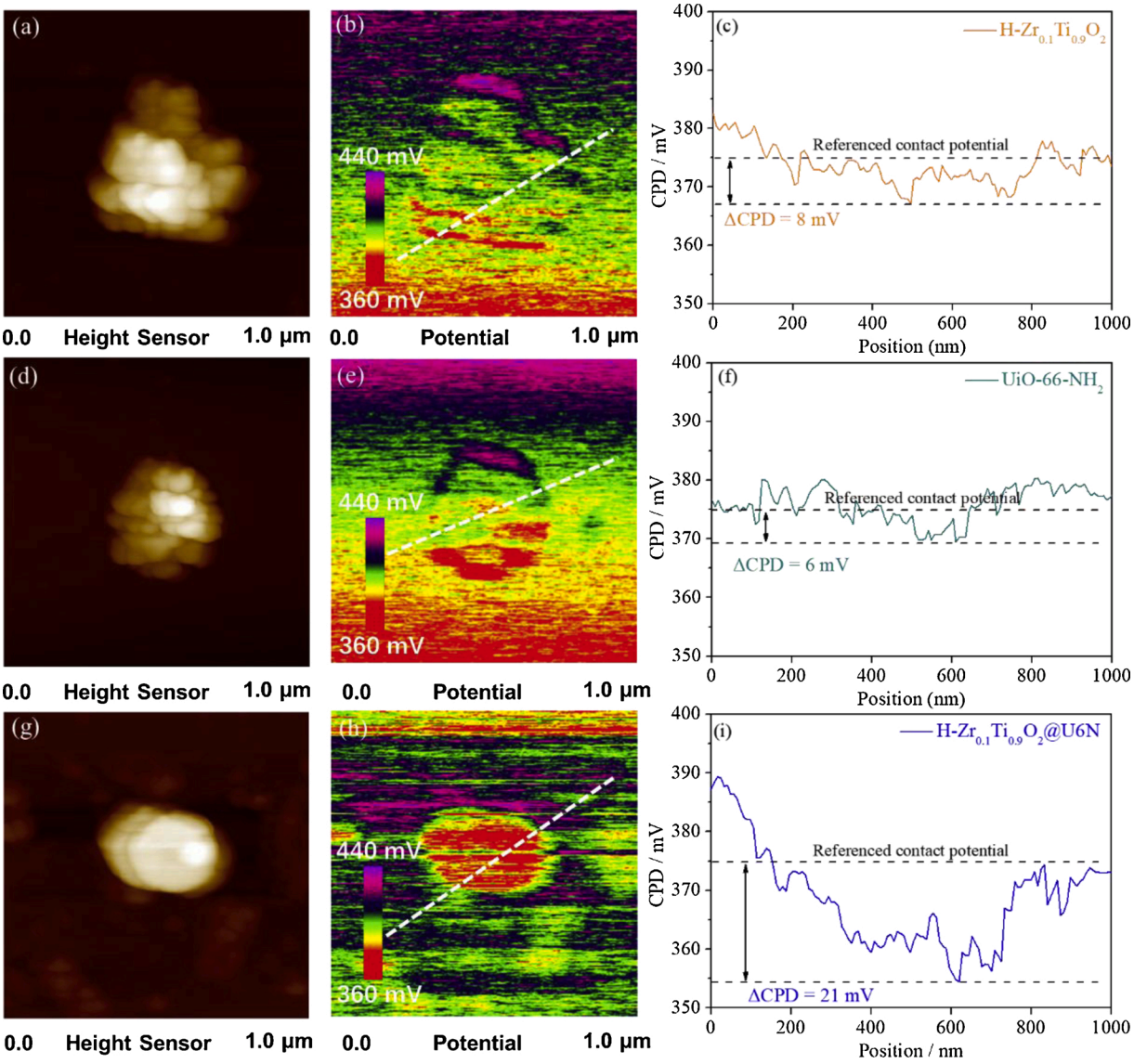

Fig. 7. *In situ* KPFM study of H-Zr0.1T0.9O2, UiO-66-NH2 and H-Zr0.1T0.9O2@U6N. AFM images showed the height of (a) H-Zr0.1Ti0.9O2, (d) UiO-66-NH2 and (g) H-Zr0.1Ti0.9O2@U6N; the images of the contact potential difference distributions of (b) H-Zr0.1T0.9O2, (e) UiO-66-NH2 and (h) H-Zr0.1Ti0.9O2@U6N; the SPV differences of the line profiles in (b), (e) and (h), respectively.

H-$Zr_{0.1}Ti_{0.9}O_2$@U6N, an apparent negative SPV sign were probed by KPFM, suggesting the accumulation of negative charges in the surface (Fig. 7h). Besides, the calculated contact potential difference (ΔCPD) of H-$Zr_{0.1}Ti_{0.9}O_2$@U6N was determined to be about 21 mV *versus* the referenced contact potential (375 mV) (Fig. 7i). The obvious decline in ΔCPD values afforded a valid evidence that H-$Zr_{0.1}Ti_{0.9}O_2$@U6N exhibited rapid migration process of photoinduced electrons and outstanding separation efficiency of irradiated electrons-holes. Given the above-mentioned results, it could be reasonably deemed that Zr/Ti inter-penetrated effects and tight-bonding interface exerted a crucial function for expediting the migration of photoinduced electrons and boosting the photocatalytic activity of H-$Zr_{0.1}Ti_{0.9}O_2$@U6N.

3.8. Photocatalytic degradation mechanism

The energy band structure of photocatalysts is crucial factor to investigate the migration path of photo-induced carriers and photocatalytic performance. In this work, the flat-band potential (E_f) of one-component H-$Zr_{0.1}Ti_{0.9}O_2$ and UiO-66-NH_2 was respectively conducted through the Mott-Schottky method. As shown in Fig. 8a–b, the slope of both Mott-Schottky curves was positive, indicating that H-$Zr_{0.1}Ti_{0.9}O_2$ and UiO-66-NH_2 were n-type semiconductors [61]. It is documented that the E_f value can be determined by the point at which the slope of Mott-Schottky's curve intersects the X-axis. The E_f of H-$Zr_{0.1}Ti_{0.9}O_2$ and UiO-66-NH_2 was determined to be -0.48 V and -0.71 V (Ag/AgCl, pH = 7.0) (Fig. 8a–b), respectively. Therefore, the E_f *versus* the normal hydrogen electrode (NHE) could be calculated to be -0.28 and -0.51 V (NHE, pH = 7.0) based on the equation: $E_{NHE} = E_{Ag/AgCl} + 0.197$ [62]. It is well established that the E_f of n-type semiconductor was nearly equal to the level of conduction band (CB) [63,64], manifesting that CB potential of H-$Zr_{0.1}Ti_{0.9}O_2$ and UiO-66-NH_2 was -0.28 (Fig. 8a) and −0.51 eV (Fig. 8b), respectively. Hence, the valence band (VB) potential of H-$Zr_{0.1}Ti_{0.9}O_2$ and UiO-66-NH_2 was determined to be 2.72 and 2.17 eV based on the afore-mentioned E_{bg} estimated from UV–vis DRS spectrum (Fig. 6b). The matched band alignments between H-$Zr_{0.1}Ti_{0.9}O_2$ and UiO-66-NH_2 would make it theoretically feasible to construct the Type-II heterojunction [65], as a result, the photogenerated electrons transferred from CB of UiO-66-NH_2 to that of H-$Zr_{0.1}Ti_{0.9}O_2$, further contributing to the reduction of Ti^{4+} to Ti^{3+} species, as verified by XPS analysis [66].

Electron spin resonance (ESR) measurements and typical scavenger experiments were determined to evaluate the contribution of the main oxidative species ($\cdot O_2^-$ and ·OH) for the degradation of ALD. As described in Fig. 8c, H-$Zr_{0.1}Ti_{0.9}O_2$@U6N exhibited apparently strong characteristic quaternion troughs of DMPO-O_2^- adduct after 10 min UV–vis light irradiation. It referred that H-$Zr_{0.1}Ti_{0.9}O_2$@U6N possessed excellent reduction capability for the generation of $\cdot O_2^-$ during the photocatalytic process, which was driven by the enriched electrons migrated from UiO-66-NH_2. So, it was well-founded to affirm that the bidirectional penetrated interface and Zr-bridged interface compatibility between H-$Zr_{0.1}Ti_{0.9}O_2$ and UiO-66-NH_2 could make it beneficial to transfer photogenerated electrons from the CB of UiO-66-NH_2 to that of H-$Zr_{0.1}Ti_{0.9}O_2$. As such, the electron enrichment in the CB of H-$Zr_{0.1}Ti_{0.9}O_2$ would exert a powerful ability to expedite the reduction of adsorbed oxygen [67]. More importantly, generated Ti^{3+} species enabled the favorable adsorption of free molecule oxygen and cooperatively accelerated the generation of abundant $\cdot O_2^-$ radicals under visible light irradiation [68]. Simultaneously, the holes from VB of H-$Zr_{0.1}Ti_{0.9}O_2$ inversely injected into the VB of UiO-66-NH_2 and reacted directly with H_2O/OH^- to generate hydroxyl radical (·OH). Visibly, the quartet peak of DMPO-·OH adducts showed the strong intensity ratio of 1:2:2:1 for H-$Zr_{0.1}Ti_{0.9}O_2$@U6N (Fig. 8c). These results suggested that $\cdot O_2^-$ and ·OH

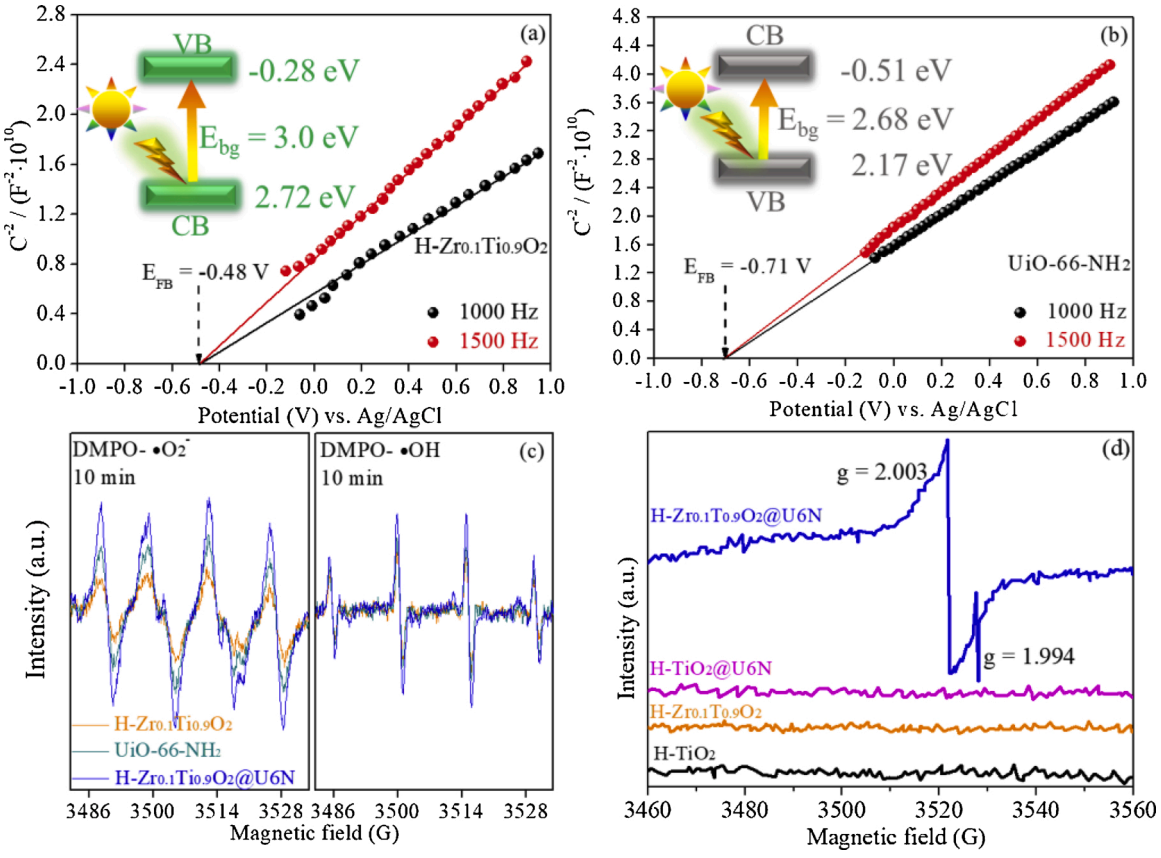

Fig. 8. Mott-Schottky curves of (a) H-Zr0.1Ti0.9O2 and (b) UiO-66-NH2; (c) ESR detection of ·O2- and ·OH generation over over the samples trapped by DMPO and (d) EPR detection of Ti3+ and oxygen vacancies.

were generated in the photocatalytic process, also confirming the fact that integrated H-$Zr_{0.1}Ti_{0.9}O_2$ with UiO-66-NH_2 would be favorable to structure "harmonious" heterojunction and promote the efficient spatial separation of electron-hole pairs. To investigate the formation of Ti^{3+} and oxygen vacancies during the reaction process, the EPR spectra of as-prepared materials were tested and shown in Fig. 8d. Clearly, the prepared H-TiO_2, H-$Zr_{0.1}Ti_{0.9}O_2$ and H-TiO_2@U6N displayed negligible EPR signals, suggesting the absence of Ti^{3+} and O_v during the reaction process. While for H-$Zr_{0.1}Ti_{0.9}O_2$@U6N, it showed a distinct EPR spectra with the g values of 2.003 and 1.994, attributing to oxygen vacancies and Ti^{3+} species [69], respectively. The results echoed well with that of XPS analysis, forcefully confirming the formation of Ti^{3+} and O_v. Subsequently, trapped experiments were explored through using the scavengers to identify the major active radicals. In this process, PBQ, EDTA-2Na and TEMPO were acted as the scavengers of $\cdot O_2^-$, h^+ and ·OH, respectively. As seen in Fig. S13a, ALD degradation was remarkably suppressed when PBQ and EDTA-2Na were added and the degradation rate decreased from 0.195 min^{-1} to 0.001 and 0.004 min^{-1} (Fig. S13b), respectively. Namely, the degradation rate was obviously decreased by ~ 99 % and ~ 98 % once adopting PBQ and EDTA-2Na as the scavengers, indicating the major roles of $\cdot O_2^-$ and h^+ in reaction system. In addition, moderate suppression is observed by adding TEMPO, suggesting that ·OH also contributed to the degradation of ALD. On the basis of these results, we can infer that $\cdot O_2^-$ and h^+ featured the predominant reactive radicals in the ALD degradation, and ·OH could be regarded as second reactive radicals to influence the ALD removal efficiency. Besides, combined with above-mentioned kinetic analysis, we deemed that effective surface adsorption and reduction of molecule oxygen on the surface of photocatalysts could be crucial rate-controlling step in the photo-catalytic process, positively facilitating the capture of photo-irradiated electrons and suppressing the carrier recombination.

Based on the aforesaid results, the possible photo-catalytic mechanism for ALD degradation over H-$Zr_{0.1}Ti_{0.9}O_2$@U6N was proposed and illustrated in Fig. 9. Under visible light irradiation, both H-$Zr_{0.1}Ti_{0.9}O_2$ and UiO-66-NH_2 could be excited and e^- would then transfer from the CB level of UiO-66-NH_2 to the CB of H-$Zr_{0.1}Ti_{0.9}O_2$ *via* the internal "Zr/Ti bridging". The generated Ti^{3+} and vacancies could structure additional energy level below the CB of H-$Zr_{0.1}Ti_{0.9}O_2$, narrowing the band gap of H-$Zr_{0.1}Ti_{0.9}O_2$ and further improving the visible light absorption. What's more, the Ti^{3+} could synergistically react with molecule oxygen to form more $\cdot O_2^-$ radicals. Meanwhile, the photo-induced holes on the VB of H-$Zr_{0.1}Ti_{0.9}O_2$ would migrate to the VB of UiO-66-NH_2 and further react with the water or hydroxide ions (OH-) to form ·OH. Eventually, the dominant radical ($\cdot O_2^-$ and h^+) would couple with ·OH to synergistically degrade ALD to nontoxic CO_2 and H_2O.

3.9. Reaction intermediates and degradation pathways

To further study the response pathways of ALD over the H-$Zr_{0.1}Ti_{0.9}O_2$@U6N, the degradation products were probed using photoacoustic detection and GC equipped with FID. As seen in Fig. 10a, the spectra of CH_3CHO clearly decreased with increasing reaction time and were almost completely decomposed within 20 min. Note that the spectra variation of ALD significantly decreased within 8 min, indicating that ALD was easily degraded. This meant that an abundant of $\cdot O_2^-$, ·OH and h^+ radicals would be generated to synergistically degrade ALD after only 8 min of light stimulation. Meanwhile, only an emerging peak appeared at a retention time of 1.02 ~ 1.03 min, corresponding to the intermediate acetic acid. Obviously, the peak took on a visible reduction within 4 ~ 8 min, attributing to the "violent attack" triggered by enhanced active radicals. Moreover, it gradually reduced to quasi horizontal range with the increase of reaction time, indicating that CH_3COOH was easily trapped and oxidized to nontoxic CO_2 and H_2O.

Fig. 10b integrated kinetic curves of CO_2 evolution over various photo-catalysts. By comparison, H-$Zr_{0.1}Ti_{0.9}O_2$@U6N exhibited nearly vertical slope within 10 min with a yielded CO_2 concentration of ~ 880 ppm, reflecting fast kinetic behavior for the degradation of ALD. Whereas, the kinetic intention appeared a gentle trend within 10 ~ 25 min, and the produced CO_2 concentration was up to 960 ppm after 20 min vis-light excitation, manifesting the nearly thorough degradation of ALD. Note that the generation time of CO_2 coincided with the degradation time of ALD (Fig. 5a), being almost synchronous to execute the photocatalytic process, indicating that the intermediate CH_3COOH existed for a very short time. The rate constant (k, min^{-1}) of CO_2 (Fig. S14a) showed that H-$Zr_{0.1}Ti_{0.9}O_2$@U6N possessed the topmost k value (0.141 min^{-1}), almost 141 times as high as that of benchmark H-TiO_2 (0.001 min^{-1}). In order to further explore the effects of the adsorption properties of materials on the photocatalytic kinetics, we conducted isothermal adsorption tests of CO_2 at 298 K and 1 bar. As shown in Fig. S14b, H-TiO_2, H-$Zr_{0.1}Ti_{0.9}O_2$ possessed an eclipsed adsorption potential for CO_2, mainly ascribing to the case of lower surface area (Table 1). While these MOFs composites showed much higher adsorption capacity of CO_2 due to their high surface area. Moreover, their adsorption capacity of CO_2 was consistent with their surface area, showing the order of U6N > H-$Zr_{0.1}Ti_{0.9}O_2$@U6N > H-TiO_2@U6N. In general, these MOF composites showed similar CO_2 adsorption ability. It indicated that kinetic adsorption was proved to be paramount for ALD degradation instead of thermodynamic adsorption in this system. Hence, the enviable kinetic motivation for the rapid generation of CO_2 were mainly ascribed to: (1) the surface affinity of H-$Zr_{0.1}Ti_{0.9}O_2$@U6N towards ALD and the effective adsorption of oxygen/water molecule, affording the continued fountainhead to produce more active radicals under light stimulation; (2) the construction of

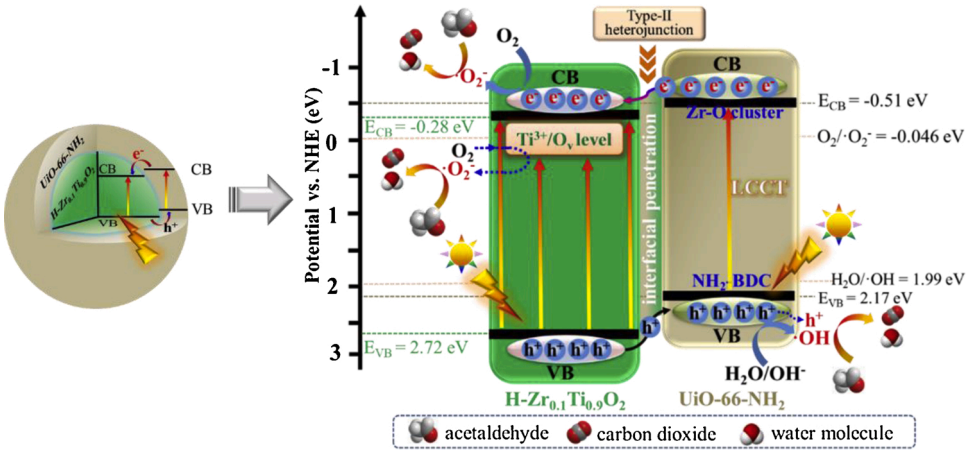

Fig. 9. Proposed photocatalytic mechanism and charge transfer for acetaldehyde degradation over H-Zr0.1Ti0.9O2@U6N photocatalysts.

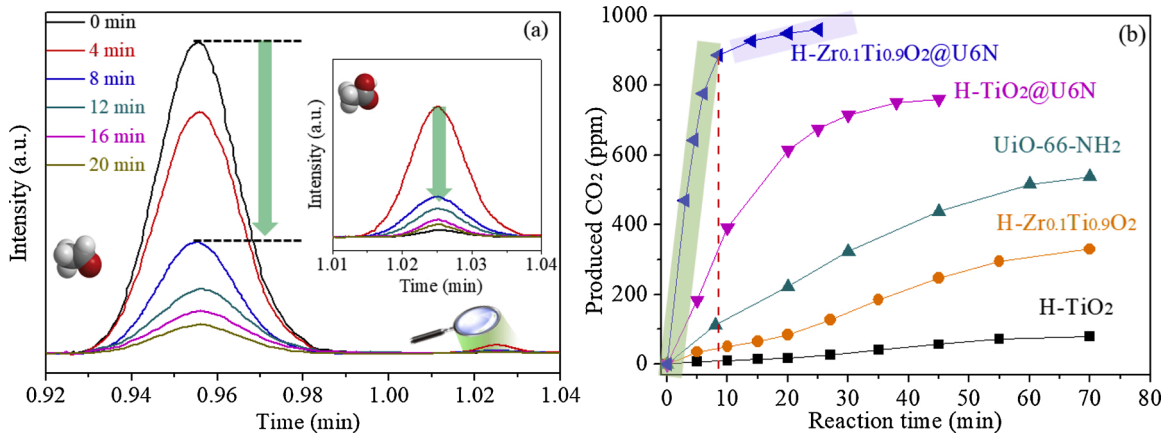

Fig. 10. (a) GC chromatograms for the photocatalytic degradation of CH3CHO over H-Zr0.1Ti0.9O2@U6N using FID detector and (b) kinetic curves of CO2 generation from CH3CHO photodegradation.

bidirectional penetrated interface would contribute to high-efficiency spatial separation of electron-hole to accelerate the formation of active radicals; (3) the intrinsic hollow geometries and interface compatibility between H-$Zr_{0.1}Ti_{0.9}O_2$ and UiO-66-NH_2 could endow CO_2 with preferable mass transfer performance.

4. Conclusions

In summary, a well-defined core-shell H-$Zr_{0.1}Ti_{0.9}O_2$@U6N having satisfied interface compatibility and bidirectional penetrated interface was successfully prepared for the photocatalytic degradation of ALD. N_2 adsorption showed that the pore geometries possessed a higher surface area of 1206.1 m^2/g with a satisfied microporous proportion of 90.2 % for H-$Zr_{0.1}Ti_{0.9}O_2$@U6N. PXRD refinements and XPS analysis suggested that Zr and Ti clusters were proved to induce the lattice expansion of H-$Zr_{0.1}Ti_{0.9}O_2$ and lattice shrink of UiO-66-NH_2, confirming the bidirectional penetrated interface between H-$Zr_{0.1}Ti_{0.9}O_2$ and U6N. PL, EIS, SPS and KPFM *etc.* analysis confirmed the salient separation properties and potential migration routine of photo-induced carriers. Thanks to the encouraging results, the photo-induced electrons and holes with high reduction and oxidation ability could positively boost the formation of active radicals including $\cdot O_2^-$, ·OH and h^+. Besides, the improved interface compatibility and internal hollow merits of H-$Zr_{0.1}Ti_{0.9}$@U6N cooperatively expedited the access of the reactants to the active sites of integrated photocatalysts, effectively shortening the "adsorption-catalysis" pathway. Degradation experiments showed that H-$Zr_{0.1}Ti_{0.9}O_2$@U6N exhibited two orders of magnitude increase of kinetics rates (195×10^{-3} min^{-1}) with a suitable RH of 75 % for degrading ALD, almost 97.5 and 16-folds enhancement compared to hollowed TiO_2 (0.002 min^{-1}) and noble metal modified photo-catalyst Ag@TiO_2 (11.9×10^{-3} min^{-1}). Furthermore, the "Interfacial metal interpenetration" strategy endowed the H-$Zr_{0.1}Ti_{0.9}O_2$@U6N with the excellent stability and durability. Hence, the newly designed H-$Zr_{0.1}Ti_{0.9}O_2$@U6N afforded novel sights for constructing improved interface compatibility over composited photocatalysts and could be deemed as valuable photocatalyst candidate for the abatement of VOCs on industrial level.

CRediT authorship contribution statement

Zhenxia Zhao and Hongbing Ji: proposed and supervised the project. **Peng Hu:** carried out the synthesis of materials, characterizations and analyzed the data. **Ruimeng Wang, Zhu Gao and Shanliang Jiang:** assisted with the analysis. **Zhenxia Zhao:** participated in the discussion of results. **Peng Hu, Zhenxia Zhao and Hongbing Ji:** co-wrote and revised the manuscript. All the authors discussed the results and participated in analyzing the experimental results.

Declaration of Competing Interest

The authors report no declarations of interest.

Acknowledgements

This work was financially supported by the National Natural Science Foundation of China (No. 21968003, 21676059, 21666004, 21938001 and 21961160741), Special Funding for 'Guangxi Bagui Scholars' Guangxi Distinguished Experts Special Foundation of China. The National Natural Science Foundation of China-SINOPEC Joint Fund (No. U1663220), the Guangdong Provincial Key R&D Program (2019B110206002), and the Local Innovative and Research Teams Project of Guangdong Pearl River Talents Program (2017BT01C102).

Appendix A. Supplementary data

Supplementary material related to this article can be found, in the online version, at doi:https://doi.org/10.1016/j.apcatb.2021.120371.

References

[1] M. Zhu, Y. Muhammad, P. Hu, B. Wang, Y. Wu, X. Sun, Z. Tong, Z. Zhao, Appl. Catal. B-Environ. 232 (2018) 182–193.
[2] Z. Gao, J. Wang, Y. Muhammad, Y. Zhang, S.J. Shah, Y. Hu, Z. Chu, Z. Zhao, Z. Zhao, Chem. Eng. J. 388 (2020).
[3] T. Salthammer, S. Mentese, R. Marutzky, Chem. Rev. 110 (2010) 2536–2572.
[4] Z. Jin, Q. Zhang, L. Hu, J. Chen, X. Cheng, Y. Zeng, S. Ruan, T. Ohno, Appl. Catal. B-Environ. 205 (2017) 569–575.
[5] J. Pan, Z. Dong, B. Wang, Z. Jiang, C. Zhao, J. Wang, C. Song, Y. Zheng, C. Li, Appl. Catal. B-Environ. 242 (2019) 92–99.
[6] J. Ryu, S. Kim, H.I. Kim, E. Jo, Y.K. Kim, M. Kim, H.D. Jang, Chem. Eng. J. 262 (2015) 409–416.
[7] X. Qin, L. Jing, G. Tian, Y. Qu, Y. Feng, J. Hazard. Mater. 172 (2009) 1168–1174.
[8] H.J. Snaith, P. Hacke, Nat. Energy. 3 (2018) 459–465.
[9] P. Li, J. Li, X. Feng, J. Li, Y. Hao, J. Zhang, H. Wang, A. Yin, J. Zhou, X. Ma, B. Wang, Nat. Commun. 10 (2019).
[10] R. Li, J. Hu, M. Deng, H. Wang, X. Wang, Y. Hu, H. Jiang, J. Jiang, Q. Zhang, Y. Xie, Y. Xiong, Adv. Mater. 26 (2014) 4783.
[11] H. Furukawa, K.E. Cordova, M. O'Keeffe, O.M. Yaghi, Science 341 (2013) 974.
[12] A. Crake, K.C. Christoforidis, A. Kafizas, S. Zafeiratos, C. Petit, Appl. Catal. B-Environ. 210 (2017) 131–140.
[13] C. Wang, X. Wang, W. Liu, Chem. Eng. J. 391 (2020).
[14] F. Xiao, S. Hung, H.B. Tao, J. Miao, H.B. Yang, B. Liu, Nanoscale 6 (2014) 14950–14961.
[15] J.B. Joo, I. Lee, M. Dahl, G.D. Moon, F. Zaera, Y. Yin, Adv. Funct. Mater. 23 (2013) 4246–4254.
[16] M.R. DeStefano, T. Islamoglu, J.T. Hupp, O.K. Farha, Chem. Mater. 29 (2017) 1357–1361.
[17] M. Fang, Z. Chen, Y. Liu, J. Quan, C. Yang, L. Zhu, Q. Xu, Q. Xu, J. Mater. Chem. A. 6 (2018) 1630–1638.
[18] J. Cai, X. Wu, S. Li, F. Zheng, ACS Sustain. Chem. Eng. 4 (2016) 1581–1590.
[19] H.J. Lee, W. Cho, M. Oh, Chem. Commun. 48 (2012) 221–223.

[20] A.D. Roddick-Lanzilotta, A.J. McQuillan, J. Colloid Interface Sci. 227 (2000) 48–54.
[21] Q. Xu, Z. Guo, M. Zhang, Z. Hu, Y. Qian, D. Zhao, Crystengcomm 18 (2016) 4046–4052.
[22] L. Zhang, Q. Zhang, H. Xie, J. Guo, H. Lyu, Y. Li, Z. Sun, H. Wang, Z. Guo, Appl. Catal. B-Environ. 201 (2017) 470–478.
[23] L.S. McCarty, A. Winkleman, G.M. Whitesides, Angew. Chem. Int. Edit. 46 (2007) 206–209.
[24] M. Jiang, X. Cao, D. Zhu, Y. Duan, J. Zhang, Electrochim. Acta 196 (2016) 699–707.
[25] M.J. Katz, S. Moon, J.E. Mondloch, M.H. Beyzavi, C.J. Stephenson, J.T. Hupp, O. K. Farha, Chem. Sci. 6 (2015) 2286–2291.
[26] J. Wang, Y. Yu, S. Li, L. Guo, E. Wang, Y. Cao, J. Phys. Chem. C 117 (2013) 27120–27126.
[27] A. Ayyagari, V. Hasannaeimi, H. Arora, S. Mukherjee, Sci. Rep.-UK 8 (2018).
[28] A. Crake, K.C. Christoforidis, A. Kafizas, S. Zafeiratos, C. Petit, Appl. Catal. B-Environ. 210 (2017) 131–140.
[29] Q. Huang, S. Tian, D. Zeng, X. Wang, W. Song, Y. Li, W. Xiao, C. Xie, ACS Catal. 3 (2013) 1477–1485.
[30] P.S. Awati, S.V. Awate, P.P. Shah, V. Ramaswamy, Catal Commun. 4 (2003) 393–400.
[31] M.A. Bunge, A.B. Davis, K.N. West, C.W. West, T.G. Glover, Ind. Eng. Chem. Res. 57 (2018) 9151–9161.
[32] P. Hu, Z. Zhao, X. Sun, Y. Muhammad, J. Li, S. Chen, C. Pang, T. Liao, Z. Zhao, Chem. Eng. J. 356 (2019) 329–340.
[33] L. Li, C. Xia, W. Li, A. Ji, C. Zhu, L. Zhang, Z. Wang, J. Yang, L. Mao, J. Nanomater. 2015 (2015).
[34] J. Lukac, M. Klementova, P. Bezdicka, S. Bakardjieva, J. Subrt, L. Szatmary, Z. Bastl, J. Jirkovsky, Appl. Catal. B-Environ. 74 (2007) 83–91.
[35] J. Pang, Z. Kang, R. Wang, B. Xu, X. Nie, L. Fan, F. Zhang, X. Du, S. Feng, D. Sun, Carbon 144 (2019) 321–332.
[36] L. Sun, R. Li, W. Zhan, Y. Yuan, X. Wang, X. Han, Y. Zhao, Nat. Commun. 10 (2019).
[37] J. Pan, Z. Dong, B. Wang, Z. Jiang, C. Zhao, J. Wang, C. Song, Y. Zheng, C. Li, Appl. Catal. B-Environ. 242 (2019) 92–99.
[38] V. Balakumar, H. Kim, J.W. Ryu, R. Manivannan, Y. Son, J. Mater. Sci. Technol. 40 (2020) 176–184.
[39] L. Sun, R. Li, W. Zhan, Y. Yuan, X. Wang, X. Han, Y. Zhao, Nat. Commun. 10 (2019).
[40] Y. Kuo, F. Kung, T. Su, Nanosci. Nanotechnol. Lett. 1 (2009) 37–41.
[41] P. Hu, X. Liang, M. Yaseen, X. Sun, Z. Tong, Z. Zhao, Z. Zhao, Chem. Eng. J. 332 (2018) 608–618.
[42] W. Song, L. Wang, Y. Gao, J. Deng, M. Jing, H. Zheng, J. Liu, Z. Zhao, M. Gao, Y. Wei, J. Mater. Chem. A. 6 (2018) 19241–19255.
[43] C. Zhang, C. Lei, C. Cen, S. Tang, M. Deng, Y. Li, Y. Du, Electrochim. Acta 260 (2018) 814–822.
[44] H. Feng, Z. Xu, L. Ren, C. Liu, J. Zhuang, Z. Hu, X. Xu, J. Chen, J. Wang, W. Hao, Y. Du, S.X. Dou, ACS Catal. 8 (2018) 4288–4293.
[45] H. Cui, H. Liu, J. Shi, C. Wang, Int. J. Photoenergy (2013).
[46] Y. Bai, W. Zhang, Z. Zhang, J. Zhou, X. Wang, C. Wang, W. Huang, J. Jiang, Y. Xiong, J. Am. Chem. Soc. 136 (2014) 14650–14653.
[47] Y. Wang, Z. Zhong, Y. Muhammad, H. He, Z. Zhao, S. Nie, Z. Zhao, Chem. Eng. J. 398 (2020).
[48] H. Zhai, J. Qi, X. Zhang, H. Li, L. Yang, C. Hu, H. Liu, J. Yang, Nanoscale Res. Lett. 12 (2017).
[49] X. Shi, M. Fujitsuka, S. Kim, T. Majima, Small 14 (2018).
[50] C. Lu, L. Shi, Y. Chen, Y. Xie, C.T. Simmons, Water Resour. Res. 52 (2016) 3637–3653.
[51] C. Lu, P.K. Kitanidis, J. Luo, Water Resour. Res. 45 (2009).
[52] Q. Zeng, X. Xie, X. Wang, Y. Wang, G. Lu, D.Y.H. Pui, J. Sun, Chem. Eng. J. 341 (2018) 83–92.
[53] X. Dong, W. Cui, H. Wang, J. Li, Y. Sun, H. Wang, Y. Zhang, H. Huang, F. Dong, Sci. Bull. 64 (2019) 669–678.
[54] A.S. Ahmed, S.M. Muhamed, M.L. Singla, S. Tabassum, A.H. Naqvi, A. Azam, J. Lumin. 131 (2011) 1–6.
[55] Y. Xu, S. Wu, P. Wan, J. Sun, Z.D. Hood, RSC Adv. 7 (2017) 32461–32467.
[56] X. He, H. Fang, D.J. Gosztola, Z. Jiang, P. Jena, W. Wang, ACS Appl. Mater. Inter. 11 (2019) 12516–12524.
[57] D. Liu, Y. Lv, M. Zhang, Y. Liu, Y. Zhu, R. Zong, Y. Zhu, J. Mater. Chem. A. 2 (2014) 15377–15388.
[58] F. Raziq, Y. Qu, M. Humayun, A. Zada, H. Yu, L. Jing, Appl. Catal. B-Environ. 201 (2017) 486–494.
[59] C. Li, M. Gao, X. Sun, H. Tang, H. Dong, F. Zhang, Appl. Catal. B-Environ. 266 (2020).
[60] Y. Wu, H. Wang, W. Tu, Y. Liu, S. Wu, Y.Z. Tan, J.W. Chew, Appl. Catal. B-Environ 233 (2018) 58–69.
[61] J. Zheng, L. Zhang, Appl. Catal. B-Environ. 237 (2018) 1–8.
[62] J. Xiong, X. Li, J. Huang, X. Gao, Z. Chen, J. Liu, H. Li, B. Kang, W. Yao, Y. Zhu, A Appl. Catal. B-Environ. 266 (2020).
[63] J. Lee, Z. Li, L. Zhu, S. Xie, X. Cui, Appl. Catal. B-Environ. 224 (2018) 715–724.
[64] J. Pan, Z. Dong, B. Wang, Z. Jiang, C. Zhao, J. Wang, C. Song, Y. Zheng, C. Li, Appl. Catal. B-Environ. 242 (2019) 92–99.
[65] B. Chai, J. Yan, G. Fan, G. Song, C. Wang, J. Alloys Compd. 802 (2019) 301–309.
[66] Z. Yang, X. Xu, X. Liang, C. Lei, Y. Cui, W. Wu, Y. Yang, Z. Zhang, Z. Lei, Appl. Catal. B-Environ. 205 (2017) 42–54.
[67] H. Hori, M. Takashima, M. Takase, M. Kitamura, F. Amano, B. Ohtani, Catal. Today 303 (2018) 341–349.
[68] Y. Cao, H. Tan, T. Shi, T. Tang, J. Li, J. Chem. Technol. Biot. 83 (2008) 546–552.
[69] M. Hu, Z. Xing, Y. Cao, Z. Li, X. Yan, Z. Xiu, T. Zhao, S. Yang, W. Zhou, Appl. Catal. B-Environ. 226 (2018) 499–508.
[70] Y. Chen, K. Katsumata, Y. Chiu, K. Okada, N. Matsushita, Y. Hsu, Appl. Catal. A-Gen. 490 (2015) 1–9.
[71] W. Lin, X. Xie, X. Wang, Y. Wang, D. Segets, J. Sun, Chem. Eng. J. 349 (2018) 708–718.
[72] Q. Zeng, X. Xie, X. Wang, Y. Wang, G. Lu, D.Y.H. Pui, J. Sun, Chem. Eng. J. 341 (2018) 83–92.
[73] Z. Lu, L. Zeng, W. Song, Z. Qin, D. Zeng, C. Xie, Appl. Catal. B-Environ. 202 (2017) 489–499.
[74] Y. Yamaguchi, S. Usuki, K. Yamatoya, N. Suzuki, K. Katsumata, C. Terashima, A. Fujishima, A. Kudo, K. Nakata, RSC Adv. 8 (2018) 5331–5337.